Single-molecule imaging reveals the kinetics of non-homologous end-joining in living cells

Mariia Mikhova [1,2], Noah J. Goff [3,4], Tomáš Janovič [2], Joshua R. Heyza [2], Katheryn Meek [3,4], Jens C. Schmidt [2,5]*

[1] Department of Biochemistry and Molecular Biology, [2] Institute for Quantitative Health Science and Engineering, [3] Department of Microbiology, Genetics, and Immunology, [4] Department of Pathobiology & Diagnostic Investigation, [5] Department of Obstetrics, Gynecology and Reproductive Biology, Michigan State University, East Lansing.

*Correspondence: schmi706@msu.edu (Twitter: @jenscs83)

SUMMARY

Non-homologous end joining (NHEJ) is the predominant pathway that repairs DNA double-stranded breaks (DSBs) in vertebrates. However, due to challenges in detecting DSBs in living cells, the repair capacity of the NHEJ pathway is unknown. The DNA termini of many DSBs must be processed to allow ligation while minimizing genetic changes that result from break repair. Emerging models propose that DNA termini are first synapsed ~115Å apart in one of several long-range synaptic complexes before transitioning into a short-range synaptic complex that juxtaposes DNA ends to facilitate ligation. The transition from long-range to short-range synaptic complexes involves both conformational and compositional changes of the NHEJ factors bound to the DNA break. Importantly, it is unclear how NHEJ proceeds *in vivo* because of the challenges involved in analyzing recruitment of NHEJ factors to DSBs over time in living cells. Here, we develop a new approach to study the temporal and compositional dynamics of NHEJ complexes using live cell single-molecule imaging. Our results provide direct evidence for stepwise maturation of the NHEJ complex, pinpoint key regulatory steps in NHEJ progression, and define the overall repair capacity NHEJ in living cells.

INTRODUCTION

DNA, the blue-print of life, is remarkably labile and can be damaged in a variety of ways. Damage that results in DNA double strand breaks (DNA breaks on both strands, DSBs) is the most toxic genomic lesion [1–3]. DSBs that are left unrepaired or repaired incorrectly can result in mutations or loss of genetic information due to chromosomal rearrangements, and, in some cases, cell death. Two major DNA double-strand break repair pathways exist in most organisms [1–3]. Non-homologous end-joining (NHEJ) directly ligates DNA ends after limited end-processing to render DNA ends chemically compatible for ligation [2]. NHEJ is active throughout the cell cycle and is estimated to repair 80% of all spontaneous DSBs in human cells [4]. Homologous recombination (HR) utilizes a sister chromatid to serve as a template DNA to repair DSBs [5]. Due to the requirement for a sister chromatid, HR functions only in the S and G2 phases of the cell cycle. In addition to engaging repair pathways, DSBs also trigger cell cycle checkpoints that temporarily or permanently halt proliferation or lead to apoptosis of the damaged cell, which is frequently taken advantage of by cancer therapeutics that induce DNA damage [6]. To understand how human cells respond to DNA damage it is critical to define the repair capacity of the different DNA repair pathways, i.e. the number of DNA lesions that can be repaired per unit time. However, determining the capacity of DNA repair pathways has been challenging, since it requires tracking DNA breaks over time in living cells.

The core NHEJ factors include Ku70, Ku80, DNA-PKcs, XLF, XRCC4 and Ligase 4 [2,7]. The highly abundant heterodimer of Ku70 and Ku80 (Ku70/80) forms a ring structure that binds double-stranded DNA ends with a high affinity [8]. Ku70/80 serves as the regulatory subunit of the DNA-dependent protein kinase (DNA-PK), which is activated when Ku70/80 binds DNA ends, resulting in recruitment of DNA-PKcs, the catalytic subunit of DNA-PK [9]. Ku70/80, and to a lesser extent DNA-PKcs, serve as a scaffold to target the other core NHEJ factors and numerous end-processing enzymes, many of which possess Ku-binding motifs that facilitate assembly of various NHEJ complexes [7,8,10].

In recent years, cryogenic electron microscopy (Cryo-EM), and *in vitro* single-molecule imaging studies have significantly advanced our understanding of the assembly mechanism underlying the recruitment of the core NHEJ factors to facilitate DSB repair [11–19]. Single-molecule Förster resonance energy transfer (FRET) studies suggest that after Ku70/80 binds DNA ends and recruits DNA-PKcs, the DNA ends are synapsed, but are positioned more than 100 Å apart in a long-range synaptic complex [16,17]. This long-range complex can progress into a short-range synaptic complex where the ends are in sufficiently close proximity to facilitate ligation. This transition requires Ku70/80, the catalytic activity of DNA-PKcs, and components of

51 the ligase complex (Lig4, XRCC4, and XLF) [17]. Recently a plethora of new cryo-EM studies has
52 provided support for this model and surprisingly defined two types of long-range complexes.
53 One long-range complex can form with only Ku70/80 and DNA-PKcs (but can also include XLF,
54 XRCC4, and Ligase4); the other long-range complex is dependent on XLF and has only been
55 observed in complexes that also include XRCC4 and Ligase 4 [11–15]. Follow-up mutational
56 analysis suggested that the different long-range complexes facilitate distinct end-processing
57 reactions that are required for the repair of DSBs with specific DNA end chemistries [19].
58 However, there is currently no direct evidence that these complexes exist in living cells.
59 Moreover, a clear understanding of how NHEJ progresses *in vivo* is lacking. A key challenge
60 has been the lack of tools to study the binding of NHEJ factors to chemically well-defined breaks
61 in living cells. Live cell imaging of laser micro-irradiation (LMI) induced DNA damage has been a
62 useful approach to visualize the recruitment of DNA repair factors to spatially and temporally
63 well controlled DNA lesions in real time [20-22]. However, LMI induces complex DNA lesions that
64 include DSBs, single-strand breaks, and base damage and the relative contribution of the
65 various types of DNA damage to the recruitment of the repair factors is impossible to
66 disentangle [23-25]. In addition, because only two to four copies of each NHEJ factor are expected
67 to be recruited to a single DSB, the accumulation of NHEJ factors at DNA lesions is difficult to
68 detect in living cells.
69 In this study, we address these challenges by developing a single-molecule imaging method
70 to analyze the recruitment of endogenously HaloTagged NHEJ factors to chemically induced
71 DNA breaks. We define the recruitment dynamics of the core NHEJ factors to DSBs and
72 demonstrate that U2OS cells have the capacity to repair ~1000 DSBs per minute via the NHEJ
73 pathway. Our results reveal that Ku70/80 and DNA-PKcs are recruited to DSBs before the
74 components of the ligase complex (XRCC4, XLF, Lig4), consistent with the formation of a long-
75 range complex that only contains Ku70/80 and DNA-PKcs. In addition, we observe that DNA-
76 PKcs dissociates from DSBs ~10 minutes prior to Ku70/80, XLF, and XRCC4. This provides
77 direct evidence for the presence of DNA-PKcs free, long-lived short-range synaptic complexes
78 in cells, and suggests a subset of breaks require extensive processing prior to ligation.
79 Importantly, the dissociation of DNA-PKcs requires its catalytic activity, and its inhibition
80 prevents the release of all other NHEJ factors analyzed, consistent with an arrest of NHEJ
81 progression. Finally, we analyze the role of Ligase 4 in NHEJ complex maturation. In the
82 absence of Ligase 4, the long-range synaptic complex containing XLF and the XRCC4-Ligase 4
83 fails to form, and Ku70/80 and DNA-PKcs rapidly dissociate from DNA breaks. In addition,
84 consistent with previous in vitro studies, the catalytic activity of Ligase 4 is not required for short-

range complex formation, but delays the removal of DNA-PKcs, indicating that the interaction of Ligase 4 with DNA substrate might contribute to the transition to the short-range synaptic complex. Altogether our work provides direct evidence for the existence of NHEJ complexes with distinct compositions in living cells, precisely determines their maturation over time and defines the repair capacity of the non-homologous end joining pathway in cancer cells.

RESULTS

Generation of functional, endogenously HaloTagged NHEJ factors

To facilitate live cell single-molecule imaging of NHEJ factors, CRISPR-Cas9 and homology-directed repair were used to insert the sequence encoding a 3xFLAG-HaloTag (Halo) at the N-terminus of the endogenous *Ku70*, *DNA-PKcs* (generated in our previous work [26]), *XLF*, and *XRCC4* loci in U2OS cells (Fig. 1A). For each gene, all alleles were edited, the insertions were

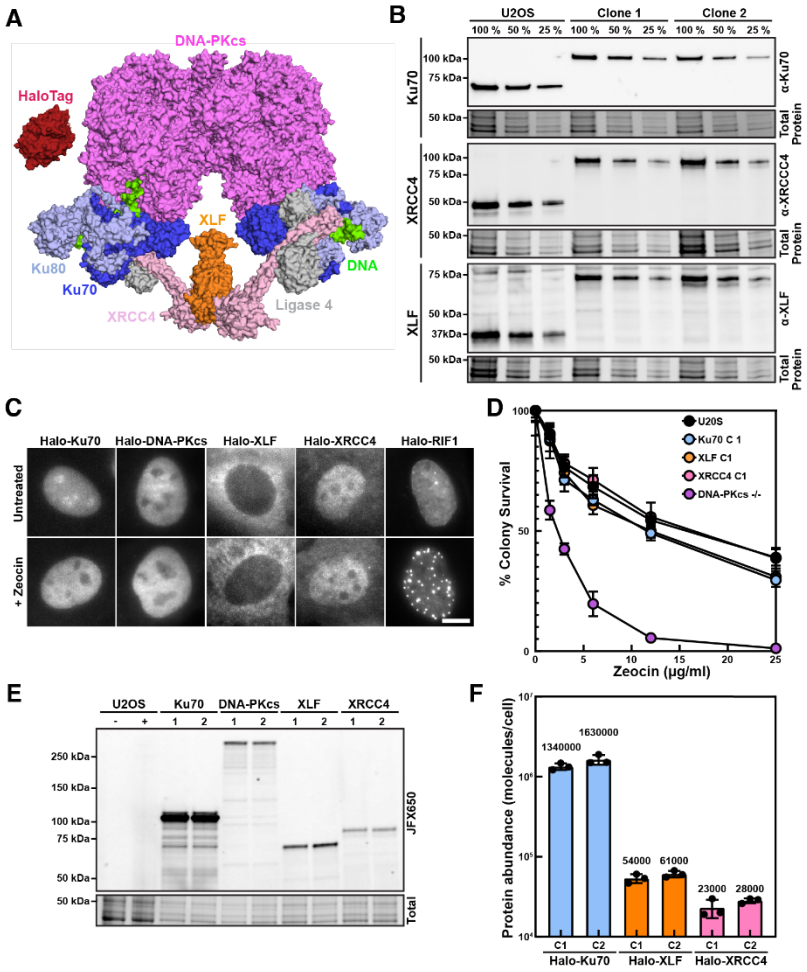

Figure 1. Generation and validation of HaloTagged core NHEJ proteins in U20S cells.
(A) Graphical depiction of the long-range XLF-mediated NHEJ synaptic complex and HaloTag (based on PDB: 7NFC and 6U32) [13,44]. **(B)** Western blots of U2OS cells expressing HaloTagged NHEJ factors and parental U2OS cells probed with antibodies against Ku70 (top), XRCC4 (middle), and XLF (bottom). **(C)** Representative images of living cells expressing HaloTagged NHEJ factors and Halo-Rif1 labeled with JFX650 HaloTag ligand in the presence or absence of zeocin (Scale bar = 10 um). **(D)** Clonogenic survival assay of U2OS cells expressing HaloTagged NHEJ factors, parental U2OS cells, and U2OS cells with DNA-PKcs knocked out after challenge with Zeocin (N = 4, 3 technical replicates per biological replicate, Mean ± S.D.). **(E)** Fluorescence imaging of 2 clones of each HaloTagged NHEJ factor labeled with JF650 HaloTag ligand and separated on an SDS-PAGE gel. **(F)** Quantification of the total protein abundance based on recombinant 3X FLAG-HaloTag labeled with JF646 and cell lysates from a specific number of U2OS using in-gel fluorescence intensity values after applying a correction factor from western blots (see Fig. S1C-D, N = 3, Mean ± S.D.).

96 verified using Sanger sequencing, and exclusive expression of the tagged protein was
97 confirmed using western blot (Fig. 1B). To assess subcellular localization of the HaloTagged
98 NHEJ factors, cells were labeled with a fluorescent HaloTag ligand (JFX650), and the tagged
99 proteins were visualized using widefield fluorescence microscopy. In the presence or absence
100 of the DSB-inducing drug zeocin, Halo-Ku70, Halo-DNA-PKcs, and Halo-XRCC4 localized
101 exclusively to the nucleus (Fig. 1C). In contrast, Halo-XLF was detected in both the cytoplasm
102 and the nucleus, consistent with previous observations by others [27]. To further confirm the
103 cytoplasmic localization of XLF, we performed cellular fractionations of parental U2OS and the
104 Halo-XLF cell line. Both wildtype XLF and Halo-XLF are present in cytoplasm and nucleus (Fig.
105 S1A), demonstrating that XLF cellular localization is not limited to the nucleus in U20S cells.
106 Notably, Halo-DNA-PKcs, Halo-XLF, and Halo-XRCC4 were excluded from nucleoli (Fig. 1C). In
107 contrast, in the absence of DNA damage, Halo-Ku70 was present in both the nucleoplasm and
108 enriched in nucleoli (Fig. 1C). However, in the presence of Zeocin, Halo-Ku70 appeared to be
109 evicted from nucleoli (Fig. 1C), consistent with observations by others [28]. Importantly, none of
110 the NHEJ factors formed DNA repair foci after induction of DSBs using zeocin, while Halo-Rif1
111 repair foci were readily detectable after DSBs induction, as expected [29]. To assess whether the
112 HaloTag disrupts cellular function of the tagged NHEJ factors, we carried out clonogenic
113 survival assays. Zeocin resistance in the four HaloTagged NHEJ factor cell lines was
114 comparable to parental U2OS cells, while DNA-PKcs knock-out cells were highly sensitive to
115 Zeocin (Fig. 1D, Fig. S1B). We conclude that the N-terminal fusion of the 3xFLAG-HaloTag
116 does not significantly alter the DNA repair function of Ku70, DNA-PKcs, XRCC4, or XLF.
117

118 **Absolute cellular abundance of Ku70, XLF and XRCC4**

119 To determine the absolute cellular abundance of Ku70, XLF, and XRCC4 we compared the
120 fluorescence intensity of labeled Halo-Ku70 and Halo-XRCC4 bands on SDS-PAGE gels to that
121 of a standard containing a known quantity of recombinant 3xFLAG-HaloTag protein labeled with
122 the same fluorophore and a cell lysate from a specified number of cells (Fig. S1C-D). The
123 absolute abundance of Halo-XLF was determined by comparing the fluorescence intensity of
124 Halo-XLF to that of Halo-XRCC4 normalized to total protein loaded (Fig. 1E). To calculate the
125 absolute abundance of endogenous, untagged proteins the absolute abundance of the
126 HaloTagged variants was multiplied by the relative expression of the HaloTagged proteins
127 compared to their untagged counterparts determined by western blot (Fig. 1B). As previously
128 described, the expression level of Ku70 is very high (1.3 - 1.6x10^6 molecules per cell) [30].The
129 expression levels of XLF (54 - 61x10^3 molecules per cell) and XRCC4 (23 - 28x10^3 molecules

130 per cell) were substantially lower. In previous work we determined that DNA-PKcs is present at
131 1.20×10^5 molecules per cell [26]. We confirmed the absolute protein number of the tagged NHEJ
132 factors by using a second fluorescent ligand for the HaloTag (JF657, Fig. S1E). Together these
133 observations demonstrate that the abundance of the core NHEJ factors spans two orders of
134 magnitude, with Ku70 being present in a 10-fold excess compared to DNA-PKcs, which in turn
135 is 2-5 fold more abundance than XRCC4 and XLF.

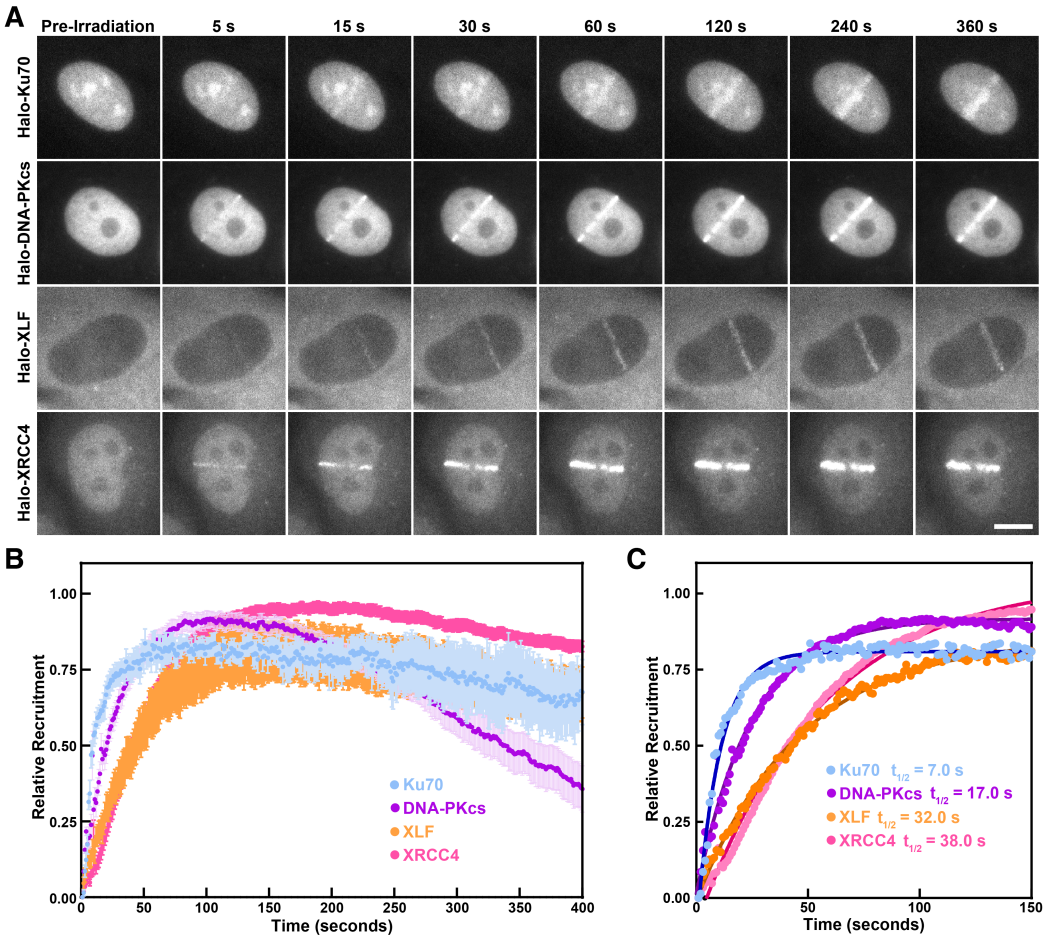

Figure 2. Recruitment kinetics of the core NHEJ factors to complex DNA lesions
(A) Representative images of HaloTagged NHEJ factor (JFX650) recruitment to laser-induced DNA lesions over time (Scale bar = 10 □m). **(B)** Normalized recruitment kinetics of HaloTagged DDR proteins to laser-induced DSBs. Data are presented as the average increase in fluorescence post-laser microirradiation normalized to the brightest frame for cell analyzed (N = 10 - 15 individual cells analyzed for each HaloTag cell line, Mean ± S.D.). (**C)** Half-times ($t_{1/2}$) of each protein to laser-induced DSBs determined by nonlinear regression assuming one-phase association (without dissociation).

136

137 **Stepwise recruitment of NHEJ factors to laser micro-irradiatation induced DNA lesions**

138 To analyze the recruitment of the tagged NHEJ factors to DNA lesions in real time, we
139 performed laser micro-irradiation (LMI) experiments using a 405 nm laser of cells sensitized with
140 Hoechst dye. While LMI induces complex DNA lesions, including DSBs, it provides consistent

141 experimental conditions (pulse length, laser power) and allows analysis of NHEJ factor
142 localization to site of DNA damage with minimal time delay after induction of DNA damage [20,25].
143 All tagged NHEJ factors were robustly recruited to LMI-induced damage sites (Fig. 2A-C, Fig.
144 S2A-D, Movie S1-4). Halo-Ku70 and Halo-DNA-PKcs were recruited to damaged sites very
145 rapidly, with a half-maximal accumulation time ($t_{1/2}$) of ~7 and ~17 seconds, respectively (Fig.
146 3C, Movie S1-2). Halo-XRCC4 and Halo-XLF were recruited with similar kinetics but were
147 delayed ($t_{1/2}$ = 32 and 38 s) compared to Halo-Ku70 and Halo-DNA-PKcs, consistent with
148 previous results (Fig. 2A-C, Movie S3-4) [31]. Similar to zeocin-induced damage, LMI also induces
149 depletion of Halo-Ku70 from nucleoli (Fig. 2A, Movie S1). These observations demonstrate that
150 the HaloTagged NHEJ factors can bind to DNA lesions and the delayed recruitment of XRCC4
151 and XLF is consistent with the initial formation of an NHEJ complex composed of only Ku70/80
152 and DNA-PKcs.
153
154 **Zeocin-induced DSB formation promotes chromatin association of Halo-tagged NHEJ**
155 **factors**
156 To analyze the diffusion dynamics of individual HaloTagged NHEJ factors, we carried out highly
157 inclined laminated optical sheet (HILO) microscopy of cells sparsely labeled with a fluorescent
158 HaloTag ligand in combination with single-particle tracking (SPT, Movie S5-S9) [20, 32,33]. Under
159 these conditions only a small fraction of the total cellular proteins was labeled, ranging from
160 0.01% for Halo-Ku70 to 0.6% for Halo-XLF (Fig. S3A-B). Analysis of single-molecule trajectories
161 using the Spot-On tool allowed us to determine the fraction of static molecules, which we
162 presume include molecules that are directly associated with chromatin, including DSBs (Fig. 3A-
163 B) [32]. In addition, Spot-On calculates the diffusion coefficients of freely diffusing molecules
164 (D_{Free}) and chromatin bound (D_{Bound}) molecules (Fig. 3B) [24]. As controls for freely diffusing and
165 chromatin bound proteins, constructs encoding only the HaloTag fused to three nuclear
166 localization sequences (Halo-NLS) and HaloTag-histone H2B (Halo-H2B) were transfected into
167 parental U2OS cells [26]. Halo-NLS diffused rapidly through the nucleus (D_{Free} = 2.6 $\mu m^2/s$) and
168 only a small fraction of molecules was static (F_{Bound} = 10%, Fig. 3C-D, Fig. S3D, Movie S5-S6).
169 In contrast and as expected, the majority of Halo-H2B was associated with chromatin (F_{Bound} =
170 80%, Fig. 3C, Fig. S3D). In the absence of DNA damage, all four HaloTagged NHEJ factors
171 displayed an intermediate level of chromatin bound molecules (F_{Bound} = 20-30%, Fig. 3C, Fig.
172 S3D, Movie S7-S9). Upon DNA damage induction with zeocin the chromatin associated fraction
173 of all tagged NHEJ factors significantly increased by 10-20% (Fig. 3C, Fig. S3D) demonstrating

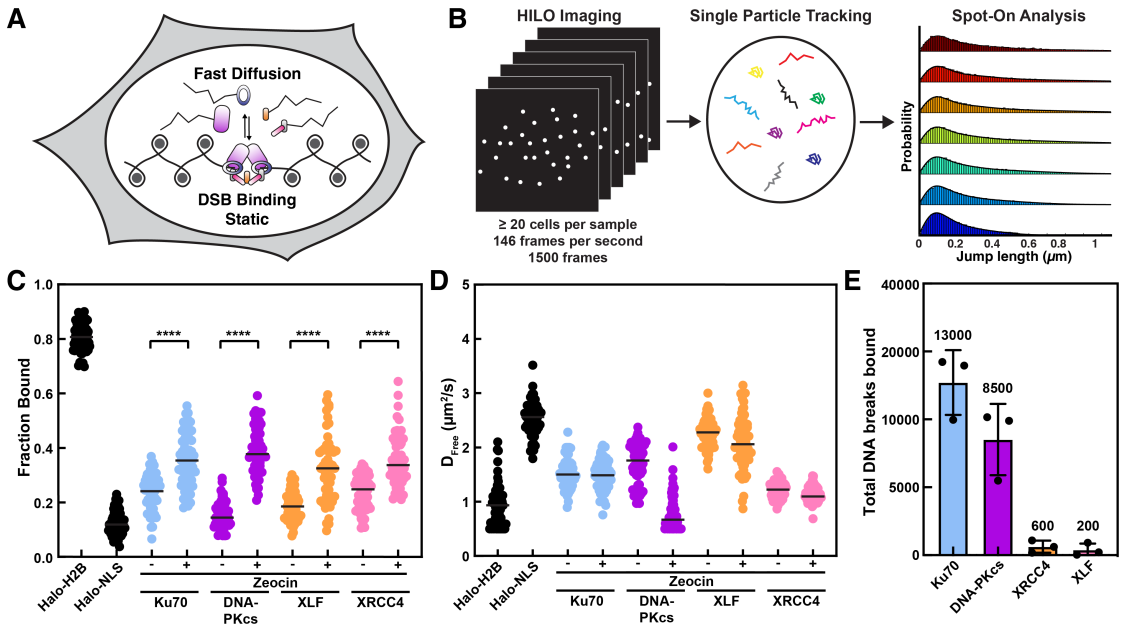

Figure 3. Zeocin-induced DSB formation promotes chromatin association of Halo-tagged NHEJ factors. **(A)** Rational for analyzing DSB association of NHEJ factors using single-molecule imaging. DSB association proteins are static while unbound molecules diffuse rapidly through the nucleus. **(B)** Graphical representation of the workflow used for live-cell single-molecule imaging of core NHEJ proteins. **(C)** Plot of the Fraction Bound for each HaloTag NHEJ protein under untreated conditions and post-zeocin exposure that were analyzed using a two-state model of diffusion. Each data point represents the fraction bound of each protein in an individual cell (N = 3, n ≥ 20 cells for each protein per replicate and condition, Black bar = median). Data were analyzed by two-way ANOVA with Tukey's posthoc test (**** = $p < 0.0001$). **(D)** Diffusion coefficients for freely diffusing HaloTagged NHEJ proteins. Each data point represents the D_{Free} calculated from the tracks in an individual cell (N = 3, n ≥ 20 cells for each protein per replicate and condition, Black bar = median). **(E)** Total number of DNA breaks bound be each tagged DNA repair factor after treatment with zeocin (N = 3, Mean ± S.D.).

that this single-molecule imaging approach can detect the recruitment of NHEJ factors to DSBs, even though DNA repair foci specific for the core NHEJ factors are generally not detectable by traditional microscopy. The increase in the chromatin bound fraction of DNA-PKcs correlated with the dose of zeocin used (Fig. S3C), consistent with the recruitment of DNA-PKcs to chromatin as a consequence of DSB formation. To confirm that Halo-DNA-PKcs was recruited to chromatin in response to DSB induction in a different cell line, we expressed Halo-DNA-PKcs in CHO-V3 cells (Chinese hamster ovary cells that lack DNA-PKcs). Similar to our observations in U2OS cells, in CHO-V3 cells the chromatin bound fraction of Halo-DNA-PKcs was also increased in response to zeocin treatment (Fig. S3E). The diffusion coefficients of freely diffusing Halo-Ku70, Halo-DNA-PKcs, and Halo-XRCC4 were comparable in the absence of DNA damage (D_{Free} = 1.6-1.9 $\mu m^2/s$, Fig. 3D). Halo-XLF diffused more rapidly through the nucleus (D_{Free} = 2.5 $\mu m^2/s$), indicating that it does not constitutively associate with the other NHEJ factors, in particular XRCC4. The diffusion coefficients of freely diffusing and chromatin bound Halo-Ku70, Halo-XRCC4, and Halo-XLF molecules were not affected by DSBs induction

188 using zeocin (Fig. 3D, Fig. S3F). In contrast, the D_{Free} of Halo-DNA-PKcs was reduced to D_{Free} =
189 0.7 $\mu m^2/s$ after zeocin treatment (Fig. 3D). Similarly, the D_{Bound} of of Halo-DNA-PKcs was also
190 reduced after DSB induction (Fig. S3E). This suggests that DNA-PKcs globally transitions into a
191 different macro-molecular complex after DNA damage induction, or it forms many transient
192 interactions with chromatin that slow down its diffusion dynamics.
193 In addition to defining the diffusion dynamics of the HaloTagged NHEJ factors, these
194 experiments allowed us to estimate the number of DNA breaks bound by each tagged NHEJ
195 factor per cell. The number of chromatin-bound molecules was determined by multiplying the
196 increase in the static fraction upon zeocin treatment ($F_{bound\ zeocin} - F_{bound\ Untreated}$) with the average
197 number of molecules detected per imaging frame for each protein. This number was then
198 divided by the labeling efficiency to account for the small fraction of molecules that are
199 detectable (Fig. S3B). In addition, we multiplied the number by 3 because we only sample a 1
200 µm thick plane of the cell nucleus, which is 4 µm in height (Fig. S3G, see methods for details) [34].
201 Finally, the resulting number was divided by the number of molecules expected to be present at
202 a single DSB (2 for Ku70 and DNA-PKcs, 4 for XRCC4, 2 for XLF, see Fig. 1A). Assuming the
203 increase in the fraction of chromatin-bound molecules after zeocin treatment is exclusively the
204 result of DSB binding, Halo-Ku70 and DNA-PKcs were associated with 13000 and 8500 breaks
205 per cell (Fig. 3E), respectively. Halo-XRCC4 and Halo-XLF only associated with 600 and 200
206 DSBs per cell (Fig. 3E), respectively. These numbers are consistent with the hierarchy of NHEJ
207 factor recruitment, and the relative abundance of the tagged proteins.
208 Altogether, these results demonstrate that single-molecule imaging can be used to study
209 the recruitment of NHEJ factors to DSBs in living cells and to estimate the total number of
210 breaks bound by each protein analyzed.
211
212 **Kinetics of NHEJ factor recruitment to Calicheamicin induced DSBs**
213 To determine the kinetics of chromatin association of the HaloTagged NHEJ factors, SPT was
214 used to analyze recruitment to calicheamicin induced DSBs; calicheamicin mostly induces DNA
215 breaks with 3' overhangs, a high percentage of which have 3' phospho-glycolate adducts [35,36].
216 Cultures of cells expressing Halo-Ku70, Halo-DNA-PKcs, and Halo-XRCC4 were treated with
217 various concentrations of calicheamicin for 3 minutes and individual cells were imaged for ~10
218 seconds each in one-minute intervals, before and after damage induction to determine the
219 fraction of chromatin bound molecules (Fig, 4A, Movie S10, each data point represents a
220 different cell). Prior to treatment with calicheamicin the fraction of chromatin bound molecules
221 remained constant for all NHEJ factors (Fig. 4B, Movie S10). After DNA damage induction the

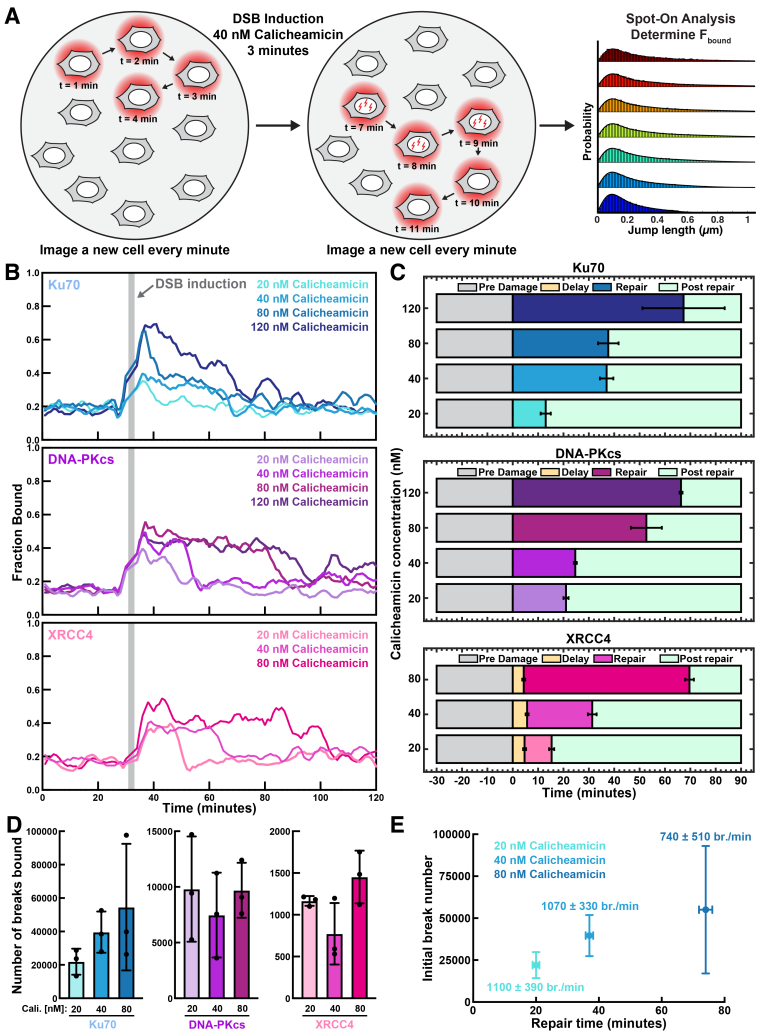

Figure 4. Time course analysis of the recruitment of Halo-tagged NHEJ factors to DNA breaks. **(A)** Experimental approach to analyze the chromatin binding of the tagged DNA repair factors over time. **(B)** Plot of the static fraction of Halo-Ku70, Halo-DNA-PKcs, and Halo-XRCC4 before and after DNA damage induction (shaded area) with various concentrations of calicheamicin for 3 minutes. Graphs represent the rolling average over three consecutive timepoints (for individual graphs with experimental error see Figure S4A). **(C)** Quantification of the timing of the recruitment of Halo-Ku70, Halo-DNA-PKcs, and Halo-XRCC4 after DNA damage induction (N = 3, Mean ± S.D.). **(D)** Quantification of the number of break bound Halo-Ku70 (pooled data for 5 time points after DNA damage induction), Halo-DNA-PKcs (pooled data for 10 time points after DNA damage induction), and Halo-XRCC4 (pooled data for 10 time points after chromatin recruitment) molecules after DNA damage induction with various concentrations of calicheamicin (N = 3, Mean ± S.D.). **(E)** Quantification of the DNA repair rate by using static Halo-Ku70 as a marker for the initial number of DNA breaks (Fig. 4D) and the dissociation of XRCC4 (Fig. 4B) to mark the completion of DNA repair by NHEJ (N = 3, Mean ± S.D.)

chromatin bound fraction of Halo-Ku70, Halo-DNA-PKcs, and Halo-XRCC4 increased (Fig. 4B, Fig. S4A, Movie S10), consistent with their rapid recruitment to DSBs. Importantly, the fraction bound of Halo-DNA-PKcs cells was not increased after treatment with DMSO (Fig. S4B). In the case of Halo-Ku70 the maximal fraction bound increased as the concentration of calicheamicin was increased, and gradually decreased over time, consistent with NHEJ repairing the DSBs

228 induced by the drug treatment (Fig. 4B,C, Fig. S4A). The time frame for which the fraction
229 bound of Halo-Ku70 remained elevated was elongated with increasing calicheamicin
230 concentration, indicating that the total DSB repair time was increased (Fig. 4B-C, Fig. S4C). In
231 contrast, for Halo-DNA-PKcs and Halo-XRCC4 only small changes in the fraction of chromatin
232 bound molecules were observed as the number of breaks was increased (Fig. 4B, Fig. S4A). In
233 addition, the fraction of chromatin bound Halo-DNA-PKcs and Halo-XRCC4 remained constant
234 over an extended period of time before rapidly dropping (Fig. 4B-C, Fig. S4A,C), rather than
235 gradually decreasing as observed for Halo-Ku70 (Fig. 4B). The duration of this plateau was
236 extended with increasing calicheamicin concentration for both Halo-DNA-PKcs and Halo-
237 XRCC4 (Fig. 4C).
238 To determine the total number of DNA breaks bound by the tagged NHEJ factors, we
239 carried out the same calculations outlined above for zeocin treated cells, averaging the first 5
240 cells after calicheamicin treatment for Halo-Ku70 or the first 10 cells after DNA recruitment was
241 observed for Halo-DNA-PKcs and Halo-XRCC4. The total number of breaks bound by Halo-
242 Ku70 was elevated from 22000 to 55000 breaks per cell with increasing concentrations of
243 calicheamicin (Fig. 4D). In contrast, Halo-DNA-PKcs and Halo-XRCC4 bound to ~10000 and
244 ~1000 breaks per cell for all calicheamicin concentrations used, respectively (Fig. 4D). These
245 observations suggest that the number of breaks induced in this experiment exceeds the
246 capacity of DNA-PKcs and XRCC4 and these factors are functioning at maximum speed,
247 conceptually similar to an enzyme in the presence of large excess of substrate (Fig. S4D). In
248 contrast, the chromatin recruitment of Ku70 appears not to be saturated, consistent with Ku70
249 being present in at least a 10-fold excess compared to DNA-PKcs and XRCC4. It is important to
250 note that we are not measuring the repair timing of individual DNA breaks in this experiment
251 since we are only imaging each cell for 10 seconds. Instead, these experiments report on the
252 rate with which the aggregate of all DSBs are repaired in the cell population. In total, these
253 results are consistent with Ku70 rapidly binding most, if not all, DSBs that are induced, which
254 exceeds the total number of cellular DNA-PKcs and XRCC4 molecules (Fig. S4D). Thus, in
255 order to repair all of the DSBs in these experiments, DNA-PKcs and XRCC4 must sequentially
256 localize to breaks, explaining the extended time period during which the chromatin associated
257 fraction of these factors does not change (Fig. S4D). Consistent with this interpretation the
258 duration of the chromatin association plateaus of DNA-PKcs and XRCC4, but not their height,
259 increase with the number of DSBs induced.
260
261 **The overall repair capacity of the NHEJ pathway in human cells**

262 To define the rate of NHEJ (i.e. the number of breaks repaired per minute), we used Halo-Ku70
263 as a marker to determine the number of DNA breaks initially present after exposure to
264 Calicheamicin (Fig. 4D). To measure total repair time, the time from damage induction until
265 dissociation of Halo-XRCC4 was determined, which marks completion of DNA ligation and
266 dissociation of the XRCC4-Ligase 4 complex (Fig. 4B,C). Both the repair time and initial break
267 number increased with increasing concentrations of calicheamicin (Fig. 4B,D). The repair rate
268 after treatment with 20 nM and 40 nM of calicheamicin was identical (~1100 breaks per minute),
269 while the repair rate after break induction with 80 nM was slightly lower (~750 breaks per
270 minute) (Fig. 4E). These observations suggest that the maximal DNA break repair capacity in
271 U2OS cells is approximately 1100 DSBs per minute.
272
273 **Analysis of the relative timing of NHEJ factor recruitment reveals kinetics of short-range**
274 **synaptic complex formation**
275 To precisely determine the relative timing of the recruitment of Halo-Ku70, Halo-DNA-PKcs,
276 Halo-XRCC4, and Halo-XLF to DSBs, time course experiments were performed after induction
277 of DSBs with 40 nM Calicheamicin. While Halo-Ku70 and Halo-DNA-PKcs were recruited to
278 DSBs immediately after break induction, the chromatin recruitment of Halo-XRCC4 and Halo-
279 XLF was delayed by ~6 minutes relative to Halo-Ku70 and Halo-DNA-PKcs (Fig. 5A,B). Halo-
280 XLF was associated with around 600 DNA breaks after DSB induction with 40 nM calicheamicin
281 (Fig. S5A). This suggests that DSBs are initially bound by Ku70/80 and DNA-PKcs and XRCC4
282 and XLF are recruited at a later time point, consistent with their delayed association observed
283 using LMI (Fig. 3). Halo-DNA-PKcs dissociated from chromatin ~22 minutes after DNA damage
284 induction (Fig. 5A,B). Relative to Halo-DNA-PKcs, Halo-Ku70, Halo-XRCC4, and Halo-XLF
285 remained bound to DSBs for an additional 10 minutes (Fig. 5A,B), consistent with the formation
286 of the ligation competent short-range synaptic complex that lacks DNA-PKcs.
287 To determine whether the catalytic activity of DNA-PKcs is required for its dissociation from
288 DSBs and in turn the completion of DNA repair marked by the departure of the other NHEJ
289 factors, the experiment was repeated in the presence of an DNA-PK inhibitor (Nu7441) [37]. When
290 DNA-PKcs kinase activity was inhibited, all four NHEJ factors remained associated with
291 chromatin for >60 minutes (the end of the experiment) (Fig. 5C), suggesting that DNA-PKcs
292 target phosphorylation is required for DNA-PKcs displacement from DSBs (consistent with
293 previous in vitro studies) and potentially short-range complex formation and end ligation.
294 Importantly, this observation is consistent with the requirement for DNA-PKcs catalytic activity
295 for the transition to the short-range complex in single-molecule FRET experiments [17] . To

assess whether DNA-PKcs autophosphorylation at the ADCDE-sites, which is important for DNA-PKcs function [37–42], is required for its dissociation from DSBs, wildtype Halo-DNA-PKcs and Halo-DNA-PKcs with the ABCDE sites mutated to alanine (ABCDE mutant) were expressed in DNA-PKcs-deficient U2OS cells. Similar to Halo-DNA-PKcs in the presence of the DNA-PKcs

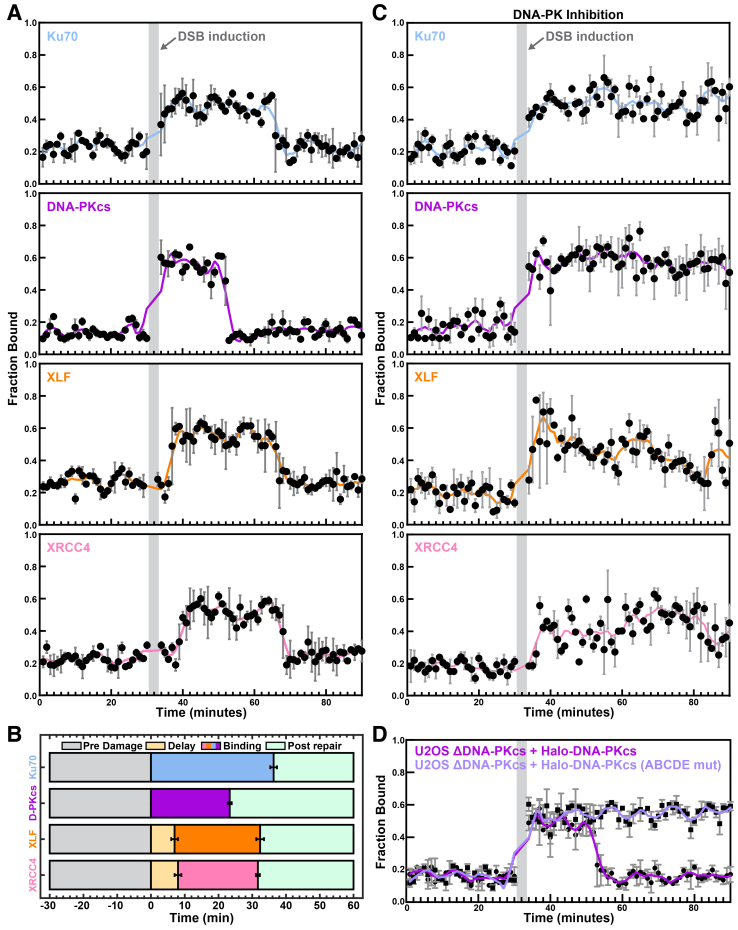

Figure 5. Compositional changes of the NHEJ complex are controlled by DNA-PK activity.
(A) Plot of the static fraction of each HaloTag NHEJ protein over time. A single cell was imaged at each timepoint. After 30 minutes DSBs were induced with 40 nM calicheamicin for 3 minutes (shaded area) and cells were imaged for 60 minutes thereafter (N = 3, Mean ± S.D.). **(B)** Quantification of the timing of the recruitment of Halo-Ku70, Halo-DNA-PKcs, Halo-XLF, and Halo-XRCC4 after DNA damage induction (N = 3, Mean ± S.D.). **(C)** Plot of the static fraction of each HaloTag NHEJ protein over time in the presence of a DNA-PK inhibitor (Nu7441, 2 nM). A single cell was imaged at each timepoint. After 30 minutes DSBs were induced with 40 nM Calicheamicin for 3 minutes (shaded area) and cells were imaged for 60 minutes thereafter (N = 3, Mean ± S.D.). **(D)** Plot of the static fraction of wildtype Halo-DNA-PKcs or Halo-DNA-PKcs with mutated autophosphorylation sites (ABCDE mut.) expressing in U2OS cells in which DNA-PKcs was knocked out. A single cell was imaged at each timepoint. After 30 minutes DSBs were induced with 40 nM calicheamicin for 3 minutes (shaded area) and cells were imaged for 60 minutes thereafter (N = 3, Mean ± S.D.).

inhibitor, the ABCDE mutant remained associated with chromatin for the entirety of the experiment, while wildtype Halo-DNA-PKcs dissociated from chromatin 20 minutes after DSB induction (Fig. 5D, Fig. S5B). These data are consistent with previous studies showing that

304 ABCDE autophosphorylation is required for DNA-PKcs dissociation from chromatin after DNA
305 damage [42,43].
306 It total, these observations in living cells are consistent with a stepwise maturation of the
307 NHEJ complex at DSBs that requires DNA-PK kinase activity; Ku70/80 and DNA-PKcs initially
308 recognize DSBs and recruit XRCC4, Lig4, and XLF. DNA-PKcs autophosphorylation-induced
309 dissociation occurs well before repair is complete, while the other core NHEJ factors remain
310 associated with the break sites, consistent with progression to the short-range synaptic
311 complexes where final repair occurs.
312
313 **Ligase 4 is required for retention of Ku70 and DNA-PKcs at DSBs and its catalytic activity**
314 **is dispensable for transition to short-range complexes.**
315 Ligase 4 has been shown to be necessary for short-range complex formation *in vitro* [17,44] . To
316 assess the role of Ligase 4 in the maturation of the NHEJ complex in living cells, Ligase 4 was
317 knocked out in cells expressing Halo-tagged Ku70, DNA-PKcs, or XRCC4 and NHEJ factor
318 recruitment to DNA breaks was analyzed after DSB induction with 40 nM Calicheamicin. Re-
319 expression of wild type Ligase 4 recapitulated the recruitment kinetics of Halo-Ku70, Halo-DNA-
320 PKcs, and Halo-XRCC4 observed in the presence of endogenous Ligase 4 (Fig. 6A,B, Fig. 5A,
321 Fig. S5C-E, Movie S11-13). In the absence of Ligase 4, Halo-Ku70 and Halo-DNA-PKcs were
322 recruited to DSBs immediately after induction and simultaneously dissociated from DNA breaks
323 after approximately 16 minutes, substantially faster than in the presence of Ligase 4 (Fig. 6A,B,
324 Fig. 5A, Fig. S5C-E, Movie S11-12). Halo-XRCC4 was not recruited to DSBs in Ligase 4
325 knockout cells (Fig. 6A, Movie S13), consistent with previous results [45,46]. These observations
326 demonstrate that Ligase 4 is required for the recruitment of XRCC4 to DNA breaks, and that
327 Ligase 4 stabilizes Ku70 and DNA-PKcs at DSBs, potentially by promoting the stability long-
328 range synaptic complexes (Fig. 1A).
329 To dissect the structural and catalytic contributions of Ligase 4 to NHEJ complex
330 formation and maturation, a previously described catalytically inactive allele of Ligase 4 (Ligase
331 4 5XK) was introduced into Ligase 4 deficient cells (Fig. S5C-E) [44]. In the presence of
332 catalytically inactive Ligase 4 both Halo-XRCC4 and Halo-Ku70 were retained at DNA breaks
333 for the entire duration of the experiment, demonstrating that DNA ends must be ligated for Ku70
334 and XRCC4 to be removed from DSBs (Fig. 6A,B). In contrast, DNA-PKcs dissociated from
335 DNA breaks, albeit after a longer delay compared to cell expressing catalytically active Ligase 4
336 (Fig. 6A, Fig. 5A). This suggests that the short-range synaptic complex can form without the
337 ability to ligate DNA ends and that DNA-PKcs dissociates from breaks prior to the

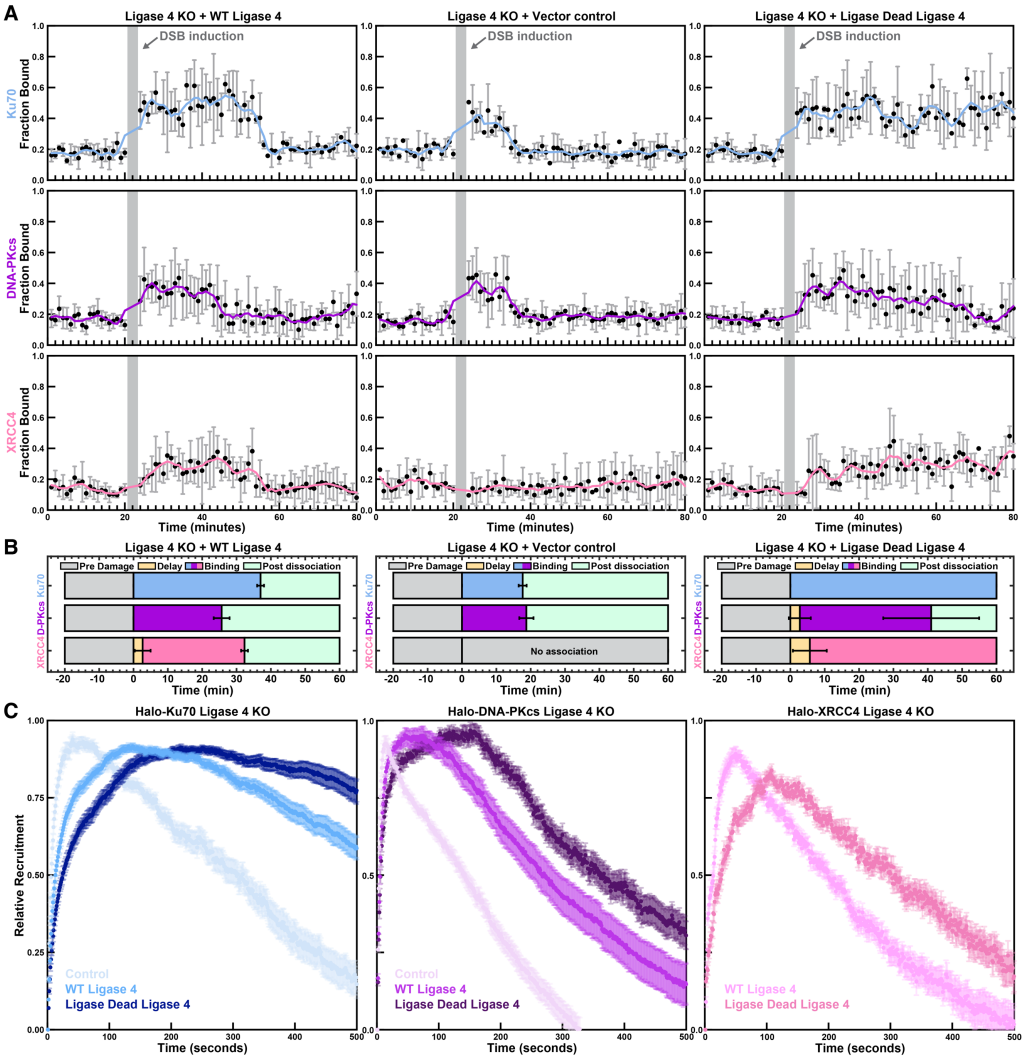

Figure 6. Ligase 4 is required for the retention of Ku70 and DNA-PKcs at DNA breaks.
(A) Plot of the static fraction of Halo-Ku70 (top row), Halo-DNA-PKcs (middle row), or Halo-XRCC4 (bottom row) over time in ligase 4 knockout cells, transiently expressing wildtype ligase 4 (left column), a vector control (middle column) or ligase dead ligase 4 (right column). After 20 minutes DSBs were induced with 40 nM Calicheamicin for 3 minutes (shaded area) and cells were imaged for 60 minutes thereafter (N = 3, Mean ± S.D.). **(B)** Quantification of the timing of the recruitment of Halo-Ku70, Halo-DNA-PKcs, Halo-XLF, and Halo-XRCC4 after DNA damage induction in Ligase 4 knockout cells expressing a control plasmid, or expression vectors for wildtype and catalytically inactive Ligase 4 (N = 3, Mean ± S.D.). **(C)** Laser micro irradiation of U2OS cells with ligase 4 knockout, expressing Halo-Ku70 (left), Halo-DNA-PKcs (middle), or Halo-XRCC4 (right), transiently expressing wildtype ligase 4, a vector control, or catalytically inactive ligase 4 (N = 30-45 cells per condition, Mean ± S.E.M.).

repair event. To confirm these observations, we carried out laser micro-irradiation experiments in Ligase 4 knockout cells expressing Halo-Ku70, Halo-DNA-PKcs, or Halo-XRCC4 transfected with a control vector or expression plasmids encoding wild type Ligase 4 or catalytically inactive Ligase 4 (Movie S14-16). Consistent with the single-molecule imaging experiments, in the absence of Ligase 4, Halo-Ku70 and Halo-DNA-PKcs rapidly dissociated from laser induced

344 DNA lesions, while Halo-XRCC4 was not recruited to sites of DNA damage (Fig. 6C, Fig. S5F-
345 G, Movie S14-16). In addition, Halo-Ku70 was retained for an extended period of time in cells
346 expressing catalytically inactive Ligase 4 (Fig. 6B, Fig. S5F). Importantly, similar to the
347 observation made by single-molecule imaging, Halo-DNA-PKcs dissociated from DNA lesions in
348 the presence of catalytically inactive Ligase 4 (Fig. 6B, Fig. S5F), consistent with the formation
349 of an NHEJ complex that lacks DNA-PKcs when DNA ligation is not possible.

350 In summary, these observations demonstrate that Ligase 4 is structurally required to
351 retain Ku70 and DNA-PKcs at DSBs and that the short-range synaptic complex that lacks DNA-
352 PKcs can form without the ability to ligate DNA ends.

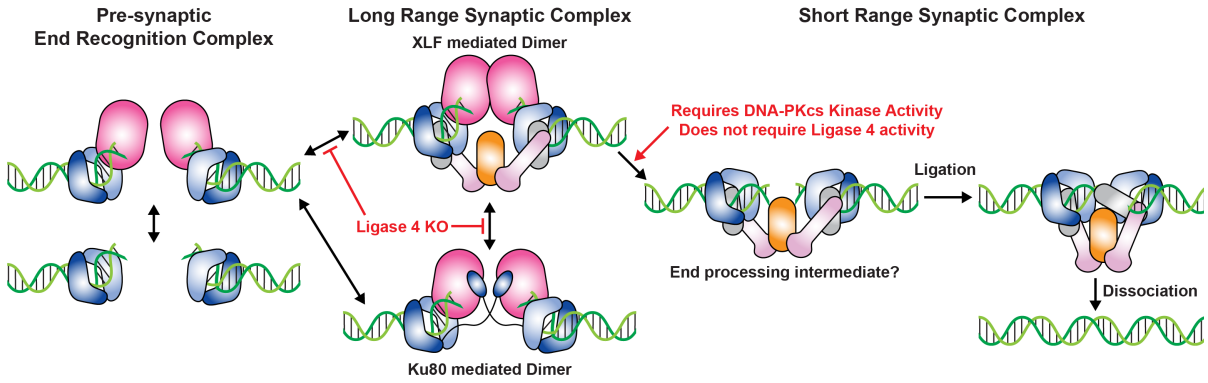

Figure 7. Model for NHEJ. Stepwise maturation of the NHEJ complex throughout DNA break repair, highlighting key transition points controlled by DNA-PKcs catalytic activity and structural contributions of the XRCC4-Ligase 4 complex.

353

354 **DISCUSSION**

355 Non-homologous end joining repairs the vast majority of DNA double strand breaks in human
356 cells. In addition to its central importance in maintaining genome integrity, toxic NHEJ can be
357 unleashed in tumors with defects in other DNA repair pathways to specifically eliminate cancer
358 cells [1,2]. Therefore, quantitatively defining the molecular mechanisms underlying NHEJ is critical
359 to understand the basic biology of DNA repair and has important clinical implications for
360 targeting DNA repair pathways as a therapeutic approach to treat cancer [467,48]. Recent single-
361 molecule FRET and Cryo-EM studies suggest that NHEJ is initiated by the formation of a long-
362 range synaptic complex, which can have several distinct compositions that likely exist in
363 equilibrium [11-15,17]. These long-range complexes transition into short-range synaptic complexes,
364 which facilitate ligation of the DNA ends, in a step that requires DNA-PK kinase activity. While
365 these elegant studies defined critical aspects of the molecular mechanism underlying NHEJ, our
366 knowledge of how NHEJ proceeds in living cells was limited.

367 Because NHEJ factors are both highly abundant and only small numbers (two to four) of the
368 core NHEJ proteins are recruited to DNA breaks, it has been challenging to detect their
369 recruitment to DSBs in living cells [20]. In addition, well established methods to analyze the
370 recruitment of DNA repair factors to sites of DNA damage in real time, for example laser micro-
371 irradiation, generate complex DNA lesions, making it difficult to interpret experimental outcomes
372 [23-25]. To overcome this hurdle, we used single-molecule live-cell imaging to study the kinetics of
373 NHEJ factors recruitment to drug induced DSBs. The key assumption is that the immobilization
374 of individual NHEJ factors in response to treatment with DNA damaging agents is caused by
375 their binding to DSBs. The single-molecule approach has two key advantages: individual
376 molecules can be detected making it possible to visualize the recruitment of factors that are not
377 present at breaks in large numbers, and small molecule drugs can be used to induce a titratable
378 number of chemically defined DNA lesions (as opposed to the complex lesions that result from
379 LMI) [20, 23-25,]. Using this approach, we analyze the temporal and compositional maturation of
380 NHEJ factors bound to DNA breaks and defined of the overall kinetics and repair capacity of the
381 NHEJ pathway in living cells.

382

383 **Repair capacity and overall rate of the non-homologous end joining pathway**

384 Our single molecule imaging-based approach to directly visualize the recruitment of NHEJ
385 factors to DNA breaks allowed enumeration of the chromatin bound DNA repair factors
386 providing an estimate of the overall rate of DSB repair by the NHEJ pathway. A key assumption
387 is that almost all breaks are rapidly bound by Ku70/80. Given the high abundance of Ku70 (>

388 10^6 molecules per cell) relative to the estimated number of breaks induced in the experiment (<
389 10^5 breaks per cell), this appears to be a reasonable assumption. Using Ku70 binding to DSBs
390 as a read out of the total breaks initially present in cells and the dissociation of the XRCC4-
391 Ligase 4 complex as the time point at which all breaks have been repaired, our experiments
392 indicate that the NHEJ pathway can repair up to 1100 DNA breaks per minute in U2OS cells.
393 Importantly, the repair rate measured after DSB induction with 20 nM and 40 nM of
394 Calicheamicin was identical, with both the break number and repair time doubling. Although the
395 individual measurements in these experiments exhibit variability, the notable concurrence in
396 repair rates across diverse experimental conditions augments our confidence in both the
397 efficacy of our approach and the validity of our interpretation. After damage induction with 80 nM
398 Calicheamicin, a slight reduction in the repair rate to ~750 breaks per minute was observed.
399 While this reduction could simply be a consequence of the large experimental error of this data
400 point it is tempting to speculate that the overall NHEJ repair rate slows down as the number of
401 breaks induced approaches the number of DNA-PKcs molecules present in the cell. Break
402 tethering and long-range synaptic complex formation requires a DNA-PKcs molecule to be
403 bound to each DNA end of a DSB. When cells were exposed to 80 nM Calicheamicin the
404 number of DSBs exceeds 50,000 per cell, which would require 100,000 DNA-PKcs molecules; a
405 number comparable to the abundance of DNA-PKcs determined in this work. Under these
406 conditions it would be possible that repair is delayed because simultaneous binding of DNA-
407 PKcs to both DNA ends is less likely.
408 While Ku70/80 likely rapidly associates with the vast majority of DNA breaks induced, our
409 results demonstrate that DNA-PKcs only binds to approximately 10000 DSBs, regardless of the
410 number of DNA breaks present. This suggests that a large number of breaks in our experiments
411 are only bound by Ku70/80 or Ku70/80 and DNA-PKcs. In addition, we observed a reduction in
412 the mobility of freely moving DNA-PKcs molecules in the nucleus (D_{Free}). This indicates that the
413 properties of DNA-PKcs are changed cell wide, once a substantial number of DNA breaks are
414 present in cells. A key unaddressed question is why DNA-PKcs does not appear to associate
415 with a large fraction of Ku70/80 bound DNA ends. One possibility is that many Ku70/80 bound
416 ends are not ideal substrates for DNA-PKcs because the DNA end is not sufficiently exposed for
417 DNA-PKcs to engage. For instance, if Ku70/80 associates with a DNA end in close proximity to
418 a nucleosome, which might require chromatin remodeling prior to DNA-PKcs binding. However,
419 we currently do not have evidence for this model and future studies are necessary to decipher
420 to mechanism by which DNA-Pkcs is recruited to Ku70/80 bound DNA ends.

421 In contrast to Ku70 and DNA-PKcs, XRCC4 and XLF were only associated with 1000 and
422 600 DNA breaks under our experimental conditions, respectively. In combination with the
423 observed repair rate of approximately 1000 breaks per minute per cell, this suggests that the
424 XRCC4-Ligase 4 complex and XLF complete their repair function in 30-60 seconds before
425 moving to the next DNA break. Our results are consistent with the hierarchy of NHEJ factor
426 recruitment to DNA breaks and indicate that the XRCC4-Ligase 4 complex and XLF are the rate
427 limiting factors that control the repair capacity of the NHEJ pathway in human cells.
428 Interestingly, we observed that the majority of Halo-XLF localized to the cytoplasm, rather than
429 the nucleus. In addition, work by others has demonstrated that phosphorylation of XLF by Akt
430 kinase promotes its export to the cytoplasm [27]. Together, these observations suggest that the
431 regulation of the subcellular localization of XLF could regulate the repair capacity of the NHEJ
432 pathway in human cells.
433 In total, we conclude that NHEJ has the maximal cellular capacity to repair approximately
434 1100 DSBs per minute. This rate is controlled by the availability of the XRCC4-Ligase 4
435 complex and XLF and end repair takes 30-60 seconds once the ligation machinery associates
436 with the DNA break.
437
438 **Stepwise maturation of the NHEJ complex in living cells**
439 Our observations demonstrate that Ku70 and DNA-PKcs are recruited to DSBs immediately
440 after their formation. In contrast the recruitment XRCC4 and its constitutive binding partner
441 Ligase 4, along with XLF, is only detectable approximately 6 minutes after the association Ku70
442 and DNA-PKcs. The observation that Ku70 and DNA-PKcs are targeted before XRCC4 and XLF
443 is consistent with an initial DNA end synapsis by the domain-swap Ku70/80-DNA-PKcs dimer.
444 This dimer can also exist bound to XRCC4, Ligase 4, and XLF, and transitions into the XLF-
445 dependent long-range complex by an unknown mechanism (Fig. 7) [12-14]. Mutational experiments
446 suggest that short-range complex formation requires prior formation of the XLF-dependent long-
447 range synaptic complex (Fig. 7) [19]. The four core NHEJ factors remain associated with DSBs for
448 ~15 minutes at which point DNA-PKcs dissociates. We believe that during the 15-minute
449 window in which all NHEJ factors analyzed are observed to be bound to DNA breaks the bulk of
450 end-joining occurs. DNA-PKcs, XRCC4, and XLF transition from one break to the next,
451 explaining why their fraction bound remains constant during this time interval, while the fraction
452 bound of Ku70 gradually decreases as breaks are repaired (Fig. S4D). Once DNA-PKcs
453 dissociates from DNA breaks, Ku70, XRCC4, and XLF remained bound to chromatin for an
454 additional 10 minutes. This suggests that a number of DNA breaks remain in a short-range

455 synaptic complex for an extended period of time, rather than being repaired in 30-60 seconds
456 after XRCC4-Ligase 4 association as outlined above. Since DNA-PKcs binding is no longer
457 observed, it is unlikely that these breaks transition back into a long-range synaptic complex (Fig.
458 7). We believe these breaks likely require extensive end processing or represent DNA lesions
459 that are incompatible with repair by NHEJ. Once these breaks are repaired or committed to an
460 alternative repair pathway all NHEJ factors dissociate from chromatin. Importantly, the
461 dissociation of DNA-PKcs requires the kinase activity of DNA-PK, specifically DNA-PKcs
462 autophosphorylation at the ABCDE sites, as previously suggested [41-43]. Moreover, upon
463 inhibition of DNA-PK catalytic activity all core NHEJ factors remain associated with DSBs,
464 demonstrating that short-range synaptic complex formation requires phosphorylation of
465 functionally relevant DNA-PK targets including the ABCDE sites, consistent with the FRET
466 studies [17].
467 An important limitation of our work is that we cannot determine the time point of long-range
468 complex formation. Graham *et al.* reported that NHEJ long-range complexes are short-lived
469 (only a few seconds) whereas short-range NHEJ complexes are considerably more stable [17].
470 We suggest that while DNA-PKcs is associated with DNA ends, numerous long-range
471 complexes form at a single DSB in an iterative fashion to facilitate different aspects of end-
472 processing. Although how each DSB is shuttled between different complexes has not been
473 determined. Emerging data suggest that DNA-PKcs's unique DNA End Blocking helix, which
474 appears to melt the DNA termini within the DNA-binding cradle, may provide a mechanism for
475 DNA-PK to sample DNA ends so that appropriate NHEJ complexes are formed depending on
476 the end chemistry of the DNA end bound [19]. Once ligatable, ends are paired within an XLF-
477 mediated dimer, DNA-PKcs autophosphorylates ABCDE sites in trans, resulting in dissociation
478 of DNA-PKcs and progression to the ligation competent short-range complex. Our observations
479 suggest that the transition into this short-range complex that lacks DNA-PKcs does not require
480 the catalytic activity of Ligase 4, consistent with single-molecule FRET studies [17]. However,
481 DNA-PKcs dissociation is substantially delayed in cells expressing catalytically inactive ligase 4,
482 which suggests that Ligase 4 and potentially its DNA binding activity contributes to the
483 conformational changes required for short-range complex formation, consistent with recent work
484 from Stinson *et al* [16].
485
486 In total, this study establishes a new methodology to analyze NHEJ factor association with
487 chemically well-defined DNA breaks at the single-molecule level. This approach allowed us to
488 define the overall repair capacity of the NHEJ pathway in human cancer cells and directly

visualized the compositional changes in the NHEJ complex during double-strand break repair in living cells.

ACKNOWLEDGMENTS

We would like to thank members of the Schmidt lab for discussions and Luke Lavis (HHMI Janelia Research Campus) for providing HaloTag dyes. This work was supported by grants from the NIH (DP2-GM142307) to J.C.S., (F32GM139292) to J.R.H., and (R01AI147634) to K.M..

AUTHOR CONTRIBUTIONS

Conceptualization: M.M, K.M., and J.C.S.; Experiments: M.M., J.R.H., N.J.G., K.M.; Data Analysis: M.M., J.R.H., T. J.; Writing—Original Draft: M.M.; Writing—Review and Editing: M.M., K.M., and J.C.S.

COMPETING INTERESTS

None declared.

505 **Materials and Methods**

506 **Cell Lines and Cell Culture**

507 U2OS cells were cultured in RPMI supplemented with 10% fetal bovine serum (FBS), 100
508 units/mL penicillin, and 100 µg/ml streptomycin. CHO-V3 cells were grown in alpha-MEM
509 containing 10% FBS, 2 mM L-glutamine, 0.1 mM non-essential amino acids, 1 mM sodium
510 pyruvate, 100 U/ml penicillin, 100 µg/ml streptomycin, and 10 µg/ml ciprofloxacin. Stable
511 transfectants of CHO-V3 cell were selected and maintained in complete medium containing 10
512 g/ml puromycin. All cells were grown at 37°C in a humidified atmosphere with 5% CO_2.
513

514 **Molecular Cloning, Plasmids and Genome Editing**

515 Endogenous tagging of Ku70, XLF, and XRCC4 was performed with CRISPR/Cas9 mediated
516 homology-directed repair (HDR) to precisely introduce HaloTag. To achieve this, sgRNAs were
517 inserted into the BbsI site of the pX330 plasmid (pX330-U6-Chimeric_BB-CBh-hSpCas9 was a
518 gift from Feng Zhang, Addgene plasmid # 42230) [49]. Each HDR donor plasmid was was
519 constructed from three DNA fragments by Gibson assembly: a left homology arm (449 bp), a
520 right homology arm (449 bp), and an insertion in-between the homology arms including a 3x
521 FLAG tag, an inverted SV40 promoter, a Puromycin resistance cassette (PuroR) flanked by
522 LoxP sites (for further selection), the HaloTag, and a TEV protease cleavage site, followed by a
523 short peptide linker sequence, as previously described [50, 51]. Homology arms were ordered as
524 G-blocks from IDT. U2OS cells were transfected with 1 µg of pX330 plasmid and 1 µg of the
525 HDR donor plasmid using 1 ug FuGene 6 (Promega). Approximately 2-3 days post-transfection,
526 edited cells were selected with 1 ug/mL puromycin. These cells were then transfected with 2 µg
527 of plasmid encoding eGFP-Cre recombinase (CAG-GFP-IRES-CRE was a gift from Fred Gage,
528 Addgene plasmid # 48201) [52]. To obtain individual clones cells were labeled with JFX650, and
529 single cells that were eGFP and JFX650 positive were sorted into 96-well cell culture plates
530 containing 50% conditioned media (media supernatant from previous cultures of U2OS cells
531 filtered through a 0.2 µm filter). For knockout of DNA-PKcs, cells were transfected with two
532 gRNA plasmids (TGCAACTTCACTAAGTCCA, GAAAAAGTACATTGAAATT). Knockout was
533 confirmed by Western blot and Sanger sequencing. For transient transfection of wild type Halo-
534 DNA-PKcs and Halo-ABCDE plasmids, 1ug of plasmid and FuGene 6 (Promega) were used.
535 CHO-V3 transfectants expressing human DNA-PKcs were derived by stably transfecting cells
536 with 10 ug expression plasmid and 1 ug pSuper-Puro with PEI. 48 hours after transfection, cells
537 were plated at limiting dilution in media containing 5ug/ml puromycin. Isolated clones were
538 screened for DNA-PKcs expression by immunoblotting. Ligase 4 KO cell lines were generated

539 using a gRNA and Cas9 nuclease targeting the coding region of Ligase 4. The gRNA
540 (CATACGTTCACCATCTAGCT) was previously cloned into pCas2a-Puro. 500 ng of plasmid
541 was transfected into $5*10^5$ cells using a Neon nucleofector (ThermoFisher, 4x10 ms pulses at
542 1230 V) and given 48 hours to recover. Clones were selected by plating limiting dilutions into 10
543 cm dishes in complete media + 2 ug/mL puromycin for 48 hours. After colonies had grown to
544 ~50 cell size, individual clones were manually transferred to a 24-well plate and allowed to grow
545 to confluency. Ligase 4 KO clones were analyzed by western blot probed with anti-Ligase 4
546 (Abcam, 26039). Ligase 4 was transiently complemented into KO cell lines by transfecting
547 500,000 cells with 100 ng of pmaxGFP (Lonza) and 500 ng of expression plasmid (empty
548 vector, pcDNA3-Ligase 4 WT, or pcDNA3 catalytically inactive Ligase 4 described as 5xK-R in
549 Goff et al. 2022) [44]. Approximately 100,000 cells/well were plated into 24-well glass-bottom
550 dishes (Cellvis, P24-1.5H-N) and allowed to recover for 48-72 hours before imaging.
551
552 **Antibodies and immunoblotting**
553 Cell extracts were prepared in 2x Laemmli buffer with β-mercaptoethanol. Proteins were
554 resolved by SDS–PAGE using Mini-PROTEAN TGX stain-free gels (BioRad), except for DNA-
555 PKcs for which homemade 6% polyacrylamide gels were used. Proteins were transferred to
556 PVDF using either a Trans-Blot Turbo system (with Turbo transfer buffer) (BioRad) or by
557 traditional wet tank transfer using CAPS Buffer with 10% Methanol (for DNA-PKcs). Antibodies
558 used in this study were anti-DNA-PKcs (1:1000 dilution) [53], anti-XLF (Invitrogen PA596310,
559 1:1000), anti-XRCC4 (Invitrogen, PA5-82264, 1:2000), anti-Ku70 (Invitrogen, MA5-12933,
560 1:1000), anti-Lamin B1 (Proteintech, 12987-1-AP), and anti-Tubulin (Proteintech, 66031-1-Ig).
561 HRP-conjugated secondary antibodies were used at 1:5000 dilutions and chemiluminescence
562 signal was produced using the Clarity western ECL substrate (BioRad) and detected using a
563 ChemiDoc imaging system (BioRad). All western blots were carried out in at least 3 technical
564 replicates and were analyzed using ImageQuant TL 8.2.
565
566 **Measurement and quantification of in-gel fluorescence and protein abundance**
567 To measure total protein abundance by in-gel fluorescence, cells were labeled for 30 minutes
568 with 500 nM JF646, JFX650, or JF657 HaloTag ligand. For the analysis the labeling efficiency
569 during single-molecule imaging experiments cells were either labeled for 30 minutes with 500
570 nM JFX650 to determine the total number of HaloTagged NHEJ factors present or using single-
571 molecule imaging labeling conditions (Halo-Ku70 100 pM for 30 seconds, Halo-DNA-PKcs 1 nM
572 for 1 minute, Halo-XRCC4 50 nM for 1 minute, Halo-XLF 10 nM for 1 min). Samples were

573 loaded and separated on Mini-PROTEAN TGX stain-free gels (BioRad) and fluorescence and
574 then total protein were detected using a BioRad Chemidoc, using the Cy5.5 filter and stain-free
575 gel detection after 45 seconds of UV activation, respectivly. For in-gel fluorescence
576 quantification of the HaloTagged proteins, we used a previously described method [26,54]. Briefly,
577 we created a standard curve using known amounts of recombinant 3X FLAG-HaloTag labeled
578 with JF646, or JF657 and cell lysates from a known number of U2OS cells to evaluate protein
579 abundance in two clones for each cell line. To account for the possibility of different expression
580 of HaloTagged proteins relative to untagged proteins, we determined the ratio of HaloTagged
581 relative to endogenous protein expression using western blot. All in-gel fluorescent SDS-page
582 gels were carried out in at least 3 technical and 3 biological replicates. All gels were analyzed
583 using ImageQuant TL 8.2. For quantification of the labeling efficiency in single-molecule imaging
584 experiments, the fluorescence signal was normalized to the total protein signal to normalize for
585 differences in loading and cell number.
586
587 **Clonogenic Survival Assays**
588 The day before zeocin treatment, 500 cells were seeded in six-well plates in triplicate. The next
589 day, cells were treated using a range zeocin (Gibco) concentrations for four hours, and then
590 media with zeoncin was replaced with fresh complete media without drug. Approximately 7–10
591 days after exposure to zeocin, 6-well plates were rinsed with PBS, and cells were fixed and
592 stained in crystal violet solution (20% ethanol and 1% w/v crystal violet). The crystal violet
593 solution was removed by carefully careful washing with water. Dry plates were imaged using the
594 Coomassie Blue filter set on a BioRad Chemidoc. Colony counts were determined using
595 ImageQuant TL 8.2. All colony survival assays were performed with 4 biological replicates.
596
597 **Live cell imaging**
598 Live cell imaging was carried out on a Olympus IX83 inverted microscope equipped with a 4-line
599 cellTIRF illuminator (405 nm, 488 nm, 561 nm, 640 nm lasers), an Excelitas X-Cite TURBO LED
600 light source, an Olympus UAPO 100x TIRF objective (1.49 NA), an Olympus UPlanApo 60x
601 TIRF oil-immersion objective (1.50 NA), a CAIRN TwinCam beamsplitter, two Andor iXon Ultra
602 EMCCD cameras or two Hamamatsu Orca BT Fusion cameras, a cellFRAP with a 100 mW 405
603 nm laser, an environmental control enclosure for temperature, CO_2, and humidity control. The
604 microscope was operated using the Olympus cellSense software.
605
606 **Laser Micro-irradiation**

607 Cells were labeled with the Halo-tag ligand JFX650 (a kind gift from the Lavis lab, Janelia
608 Farms, Ashburn, VA) at a concentration of 500 nM in complete media for 30 min at 37°C,
609 washed three times, and pre-sensitized with Hoechst (1 µg/ml) for ten minutes. The 405-nm
610 laser was directly coupled to the epifluorescence optical path of the microscope with 100x or
611 60x objective and images were acquired every second using the 630 nm LED light source. DNA
612 lesions were generated in a straight line across the nucleus by micro-irradiation with the 405-nm
613 laser at 25% laser power using 20 ms pulse. For quantitative analyses, we first cropped cells
614 and drift corrected using NanoJ in Fiji [55]. Intensity profiles of the laser micro-irradiated stripe
615 were generated using ImageJ and data was analyzed using GraphPad Prism by fitting an
616 exponential one-phase association model and one-phase decay model. For association phase
617 we fit the data points from damage induction until maximal binding was observed. For
618 dissociation we only considered data from the time point of maximal binding until the end of the
619 experiment.
620
621 **Single-molecule imaging**
622 Cells were grown on 24-well glass bottom dishes (Cellvis, P24-1.5H-N) for 24 hours prior to
623 imaging. Cells were sparsely labeled with JFX650 or JF646 dye [56,57] in complete media (Halo-
624 Ku70 100 pM for 30 seconds, Halo-DNA-PKcs 1 nM for 1 minute, Halo-XRCC4 50 nM for 1
625 minute, Halo-XLF 10 nM for 1 min) and were washed three times with fresh media and
626 incubated for an additional 15 min at 37°C (5% CO_2) to remove excess dye. Cells were treated
627 with 100 ug/mL zeocin or DMSO for one hour prior to HaloTag labeling and imaged at 146
628 frames per second for 3000 frames using the Andor 897 Ultra EM-CCD camera. For
629 calicheamicin treatment, cells were labeled and imaged for 30 minutes prior to addition of
630 calicheamicin for 3 minutes while in cellVivo chamber. Calcicheamicin was removed with at
631 least 3 quick washes with complete media. To inhibit DNA-PK cells were treated with 100 nM
632 Nu7441 for 2 hours prior to and during imaging. Cells for imaged at 179 frames per second for
633 1500 frames using the Hamamatsu Orca Fusion BT sCMOS camera. All experiments were
634 carried out in triplicate or more with at least 15 cells analyzed for each experiment.
635
636 **Analysis of Live-Cell Imaging**
637 To analyze the single-molecule particles TIFF files, we used the batch parallel-processing
638 version of SLIMFAST in MatLab 2020b [32]. For tracking, the following settings were used for all
639 the proteins: Exposure Time = 5.6 or 6.8 ms, NA = 1.49 or 1.50, PixelSize = 0.16 or 0.1083 µm,
640 Emission Wavelength = 664 nm, D_{max} = 5 $\mu m^2 s^{-1}$, Number of gaps allowed = 2, Localization

641 Error = 10^{-5}, Deflation loops = 0. We only analyzed particles located in nucleus using bright field
642 images to make a mask of nucleus in ImageJ. Using tracked particles, we determined the
643 diffusion coefficients and the bound fractions using the MATLAB version of SpotOn [32]. The
644 following settings were used: TimeGap = 5.6 or 6.8 ms, dZ = 0.700 μm, GapsAllowed = 2,
645 TimePoints = 8, JumpsToConsider = 4, BinWidth = 0.01 μm, PDF fitting. We applied a 2-state
646 model with the following settings: D_Free2_1State = [0.5 5], D_Bound2_State = [0.0001 0.5]
647 with an assumption that NHEJ factors are or chromatin bound or are freely diffusing. To
648 compare diffusion coefficients and bound fractions, we performed by two-way ANOVA analysis
649 with Tukey's posthoc test in GraphPad Prism. We analyzed either trajectories from individual
650 cells or pooled sets of cells as indicated in the text.
651
652 **Quantification of DNA break number and NHEJ rate**
653 The number of DNA breaks bound be each DNA repair factor analyzed by single-molecule
654 imaging was calculated by determining the increase in the fraction bound after DNA damage
655 induction ($F_{bound\ pre\ damage} - F_{bound\ post\ damage}$). The $F_{bound\ pre\ damage}$ was determined by pooled SpotOn
656 analysis of all cells imaged prior to damage. The $F_{bound\ post\ damage}$ was determined by pooled
657 SpotOn analysis of the first 5 cells post damage for Halo-Ku70, or the first 10 cells after
658 chromatin recruitment was observed for Halo-DNA-PKcs, Halo-XRCC4, and Halo-XLF. We only
659 used 5 cells for Halo-Ku70 because the F_{bound} for Halo-Ku70 rapidly decreased after initial
660 recruitment, while it remained constant for extended periods of time for the other factors
661 analyzed. The fraction bound was then multiplied by the average number of single molecule
662 localizations per imaging frame to determine the number of bound molecules observed, which
663 was also provided by the pooled SpotOn analysis. The number of bound molecules was then
664 divided by the labeling efficiency for each protein (Fig. S3B). Because the majority of the
665 nucleus is outside of the focal plane of the objective used in this experiment, we further adjusted
666 our number to account for the subsection of the nucleus images. The central 1 μm thick slice of
667 a sphere with a 4 μm diameter is 1/2.7 of the total volume of the sphere. Since we cannot be
668 certain that we always imaged the center of the nuclear volume we divided by 1/3 rather than
669 1/2.7 to account for the reduction in the fraction of the nucleus imaged when not imaging the
670 exact center of the nucleus. Finally, the number was divided by the number of repair factors
671 bound to each DNA break.
672
673 **Quantification of the timing of NHEJ factor recruitment to DNA breaks**

674 Bound fractions from single-molecule analysis were analyzed using custom MATLAB script. The
675 algorithm preprocessed the fraction bound values using moving average filter. Next, the
676 threshold was determined as a mean plus standard deviation of fraction bound values from all
677 replicas before the drug treatment. Finally, the start and end point of DNA repair state were
678 detected using sliding window with a length of 3 if the median of values within the window was
679 above or below the threshold, respectively.
680

681 **Cellular fractionation**

682 Cellular fractionation was performed as previously described [58]. Briefly, 20 million cells were
683 trypsinized, collected, and washed in ice-cold PBS before swelling in a hypotonic buffer (10 mM
684 HEPES pH 7.9, 10 mM KCl, 1.5 mM $MgCl_2$, and 0.5 mM DTT). Then, using a pre-cooled dounce
685 homogenizer and the tight pestle, swollen cells were ruptured with 13 strokes (VWR Cat. 62400-
686 595). The purify the nuclei, burst cells were centrifuged at 218xg for 5 min. To further improve
687 the quality of purified nuclei, the nuclear pellet was resuspended in buffer S1 (0.25 M sucrose,
688 10 mM $MgCl_2$), layered on top of buffer S2 (0.35 M sucrose, 0.5 mM $MgCl_2$) in a 15 ml falcon
689 tube, and centrifuged at 1430xg in a swinging bucket rotor for 5 min. Nuclei then were
690 resuspended in buffer S2. Samples of each fraction were analyzed by western blot.
691
692

693 **REFERENCES**

694 1. Chapman, J.R., Taylor, M.R.G., and Boulton, S.J. (2012). Playing the End Game: DNA Double-
695 Strand Break Repair Pathway Choice. Mol Cell *47*. 10.1016/j.molcel.2012.07.029.

696 2. Stinson, B.M., and Loparo, J.J. (2021). Repair of DNA Double-Strand Breaks by the
697 Nonhomologous End Joining Pathway. Annu Rev Biochem *90*. 10.1146/annurev-biochem-
698 080320-110356.

699 3. Watanabe, G., and Lieber, M.R. (2023). The flexible and iterative steps within the NHEJ pathway.
700 Prog Biophys Mol Biol *180–181*, 105–119. 10.1016/j.pbiomolbio.2023.05.001.

701 4. Karanam, K., Kafri, R., Loewer, A., and Lahav, G. (2012). Quantitative Live Cell Imaging Reveals a
702 Gradual Shift between DNA Repair Mechanisms and a Maximal Use of HR in Mid S Phase. Mol
703 Cell *47*. 10.1016/j.molcel.2012.05.052.

704 5. Jasin, M., and Rothstein, R. (2013). Repair of strand breaks by homologous recombination. Cold
705 Spring Harb Perspect Biol *5*. 10.1101/cshperspect.a012740.

706 6. Torgovnick, A., & Schumacher, B. (2015). DNA repair mechanisms in cancer development and
707 therapy. In Frontiers in Genetics (Vol. 6, Issue APR). https://doi.org/10.3389/fgene.2015.00157

708 7. Loparo, J. J. (2023). Holding it together: DNA end synapsis during non-homologous end joining.
709 DNA Repair, 130. https://doi.org/10.1016/j.dnarep.2023.103553

710 8. Grundy, G.J., Moulding, H.A., Caldecott, K.W., and Rulten, S.L. (2014). One ring to bring them all-
711 The role of Ku in mammalian non-homologous end joining. DNA Repair (Amst) *17*.
712 10.1016/j.dnarep.2014.02.019.

713 9. Anderson, C.W., and Lees-Miller, S.P. (1992). The nuclear serine/threonine protein kinase DNA-
714 PK. Crit Rev Eukaryot Gene Expr *2*.

715 10. Grundy, G.J., Rulten, S.L., Arribas-Bosacoma, R., Davidson, K., Kozik, Z., Oliver, A.W., Pearl, L.H.,
716 and Caldecott, K.W. (2016). The Ku-binding motif is a conserved module for recruitment and
717 stimulation of non-homologous end-joining proteins. Nat Commun *7*. 10.1038/ncomms11242.

718 11. Seif-El-Dahan, M., Kefala-Stavridi, A., Frit, P., Hardwick, S.W., Chirgadze, D.Y., Maia De Oliviera, T.,
719 Britton, S., Barboule, N., Bossaert, M., Pandurangan, A.P., et al. (2023). PAXX binding to the NHEJ
720 machinery explains functional redundancy with XLF. Sci Adv *9*. 10.1126/sciadv.adg2834.

721 12. Chen, S., Vogt, A., Lee, L., Naila, T., McKeown, R., Tomkinson, A.E., Lees-Miller, S.P., and He, Y.
722 (2023). Cryo-EM visualization of DNA-PKcs structural intermediates in NHEJ. Sci Adv *9*, eadg2838.
723 10.1126/sciadv.adg2838.

724 13. Chen, S., Lee, L., Naila, T., Fishbain, S., Wang, A., Tomkinson, A.E., Lees-Miller, S.P., and He, Y.
725 (2021). Structural basis of long-range to short-range synaptic transition in NHEJ. Nature *593*.
726 10.1038/s41586-021-03458-7.

727 14. Chaplin, A.K., Hardwick, S.W., Liang, S., Kefala Stavridi, A., Hnizda, A., Cooper, L.R., De Oliveira,
728 T.M., Chirgadze, D.Y., and Blundell, T.L. (2021). Dimers of DNA-PK create a stage for DNA double-
729 strand break repair. Nat Struct Mol Biol *28*. 10.1038/s41594-020-00517-x.

730 15. Chaplin, A.K., Hardwick, S.W., Stavridi, A.K., Buehl, C.J., Goff, N.J., Ropars, V., Liang, S., De
731 Oliveira, T.M., Chirgadze, D.Y., Meek, K., et al. (2021). Cryo-EM of NHEJ supercomplexes provides
732 insights into DNA repair. Mol Cell *81*. 10.1016/j.molcel.2021.07.005.

733 16. Stinson, B.M., Moreno, A.T., Walter, J.C., and Loparo, J.J. (2020). A Mechanism to Minimize Errors
734 during Non-homologous End Joining. Mol Cell *77*. 10.1016/j.molcel.2019.11.018.

735 17. Graham, T.G.W., Walter, J.C., and Loparo, J.J. (2016). Two-Stage Synapsis of DNA Ends during
736 Non-homologous End Joining. Mol Cell *61*. 10.1016/j.molcel.2016.02.010.

737 18. Amin, H., Zahid, S., Hall, C., & Chaplin, A. K. (2024). Cold snapshots of DNA repair: Cryo-EM
738 structures of DNA-PKcs and NHEJ machinery. In Progress in Biophysics and Molecular Biology
739 (Vol. 186). https://doi.org/10.1016/j.pbiomolbio.2023.11.007

740 19. Buehl, C.J., Goff, N.J., Hardwick, S.W., Gellert, M., Blundell, T.L., Yang, W., Chaplin, A.K., and
741 Meek, K. (2023). Two distinct long-range synaptic complexes promote different aspects of end
742 processing prior to repair of DNA breaks by non-homologous end joining. Mol Cell *83*.
743 10.1016/j.molcel.2023.01.012.

744 20. Heyza, J. R., Mikhova, M., & Schmidt, J. C. (2023). Live cell single-molecule imaging to study DNA
745 repair in human cells. In DNA Repair (Vol. 129). https://doi.org/10.1016/j.dnarep.2023.103540

746 21. Kim, J. S., Krasieva, T. B., Kurumizaka, H., Chen, D. J., Taylor, A. M. R., & Yokomori, K. (2005).
747 Independent and sequential recruitment of NHEJ and HR factors to DNA damage sites in
748 mammalian cells. Journal of Cell Biology, 170(3). https://doi.org/10.1083/jcb.200411083

749 22. Martinez-Pastor, B., Silveira, G. G., Clarke, T. L., Chung, D., Gu, Y., Cosentino, C., Davidow, L. S.,
750 Mata, G., Hassanieh, S., Salsman, J., Ciccia, A., Bae, N., Bedford, M. T., Megias, D., Rubin, L. L.,
751 Efeyan, A., Dellaire, G., & Mostoslavsky, R. (2021). Assessing kinetics and recruitment of DNA
752 repair factors using high content screens. Cell Reports, 37(13).
753 https://doi.org/10.1016/j.celrep.2021.110176

754 23. Kong, X., Mohanty, S. K., Stephens, J., Heale, J. T., Gomez-Godinez, V., Shi, L. Z., Kim, J. S.,
755 Yokomori, K., & Berns, M. W. (2009). Comparative analysis of different laser systems to study
756 cellular responses to DNA damage in mammalian cells. Nucleic Acids Research, 37(9).
757 https://doi.org/10.1093/nar/gkp221

758 24. Mavragani, I. v., Nikitaki, Z., Kalospyros, S. A., & Georgakilas, A. G. (2019). Ionizing radiation and
759 complex DNA damage: From prediction to detection challenges and biological significance. In
760 Cancers (Vol. 11, Issue 11). https://doi.org/10.3390/cancers11111789

761 25. Aleksandrov, R., Dotchev, A., Poser, I., Krastev, D., Georgiev, G., Panova, G., Babukov, Y.,
762 Danovski, G., Dyankova, T., Hubatsch, L., Ivanova, A., Atemin, A., Nedelcheva-Veleva, M. N.,
763 Hasse, S., Sarov, M., Buchholz, F., Hyman, A. A., Grill, S. W., & Stoynov, S. S. (2018). Protein
764 Dynamics in Complex DNA Lesions. Molecular Cell, 69(6).
765 https://doi.org/10.1016/j.molcel.2018.02.016

766 26. Heyza, J.R., Mikhova, M., Bahl, A., Broadbent, D., and Schmidt, J.C. (2023). Systematic analysis of
767 the molecular and biophysical properties of key DNA damage response factors. Elife *12*.
768 10.7554/eLife.87086.

769 27. Liu, P., Gan, W., Guo, C., Xie, A., Gao, D., Guo, J., Zhang, J., Willis, N., Su, A., Asara, J. M., Scully, R.,
770 & Wei, W. (2015). Akt-mediated phosphorylation of XLF impairs non-homologous end-joining
771 DNA repair. Molecular Cell, 57(4). https://doi.org/10.1016/j.molcel.2015.01.005

772 28. Schellenbauer, A., Guilly, M.N., Grall, R., Le Bars, R., Paget, V., Kortulewski, T., Sutcu, H., Mathé,
773 C., Hullo, M., Biard, D., et al. (2021). Phospho-Ku70 induced by DNA damage interacts with RNA
774 Pol II and promotes the formation of phospho-53BP1 foci to ensure optimal cNHEJ. Nucleic Acids
775 Res *49*. 10.1093/nar/gkab980.

776 29. Bekker-Jensen, S., Lukas, C., Kitagawa, R., Melander, F., Kastan, M.B., Bartek, J., and Lukas, J.
777 (2006). Spatial organization of the mammalian genome surveillance machinery in response to
778 DNA strand breaks. Journal of Cell Biology *173*. 10.1083/jcb.200510130.

779 30. Mimori, T., Hardin, J.A., and Steitz, J.A. (1986). Characterization of the DNA-binding protein
780 antigen Ku recognized by autoantibodies from patients with rheumatic disorders. Journal of
781 Biological Chemistry *261*, 2274–2278. 10.1016/S0021-9258(17)35929-X.

782 31. Yano, K., Morotomi-Yano, K., Wang, S., Uematsu, N., Lee, K., Asaithamby, A., Weterings, E., and
783 Chen, D.J. (2008). Ku recruits XLF to DNA double-strand breaks. EMBO Rep *9*, 91–96.
784 10.1038/sj.embor.7401137.

785 32. Hansen, A.S., Woringer, M., Grimm, J.B., Lavis, L.D., Tjian, R., and Darzacq, X. (2018). Robust
786 model-based analysis of single-particle tracking experiments with spot-on. Elife *7*.
787 10.7554/eLife.33125.

788 33. Tokunaga, M., Imamoto, N., and Sakata-Sogawa, K. (2008). Highly inclined thin illumination
789 enables clear single-molecule imaging in cells. Nat Methods *5*, 159–161. 10.1038/nmeth1171.

790 34. Koch, B., Sanchez, S., Schmidt, C. K., Swiersy, A., Jackson, S. P., & Schmidt, O. G. (2014).
791 Confinement and Deformation of Single Cells and Their Nuclei Inside Size-Adapted Microtubes.
792 Advanced Healthcare Materials, 3(11). https://doi.org/10.1002/adhm.201300678

793 35. Dedon, P.C., and Goldberg, I.H. (1992). Free-radical mechanisms involved in the formation of
794 sequence-dependent bistranded DNA lesions by the antitumor antibiotics bleomycin,
795 neocarzinostatin, and calicheamicin. Chem Res Toxicol *5*, 311–332. 10.1021/tx00027a001.

796 36. Menon, V., and Povirk, L.F. (2016). End-processing nucleases and phosphodiesterases: An elite
797 supporting cast for the non-homologous end joining pathway of DNA double-strand break repair.
798 DNA Repair (Amst) *43*, 57–68. 10.1016/j.dnarep.2016.05.011.

799 37. Leahy, J.J.J., Golding, B.T., Griffin, R.J., Hardcastle, I.R., Richardson, C., Rigoreau, L., and Smith,
800 G.C.M. (2004). Identification of a highly potent and selective DNA-dependent protein kinase
801 (DNA-PK) inhibitor (NU7441) by screening of chromenone libraries. Bioorg Med Chem Lett *14*,
802 6083–6087. 10.1016/j.bmcl.2004.09.060.

803 38. Cui, X., Yu, Y., Gupta, S., Cho, Y.-M., Lees-Miller, S.P., and Meek, K. (2005). Autophosphorylation
804 of DNA-dependent protein kinase regulates DNA end processing and may also alter double-
805 strand break repair pathway choice. Mol Cell Biol *25*, 10842–10852. 10.1128/MCB.25.24.10842-
806 10852.2005.

807 39. Ding, Q., Reddy, Y.V.R., Wang, W., Woods, T., Douglas, P., Ramsden, D.A., Lees-Miller, S.P., and
808 Meek, K. (2003). Autophosphorylation of the catalytic subunit of the DNA-dependent protein
809 kinase is required for efficient end processing during DNA double-strand break repair. Mol Cell
810 Biol *23*, 5836–5848. 10.1128/MCB.23.16.5836-5848.2003.

811 40. Goodarzi, A.A., Yu, Y., Riballo, E., Douglas, P., Walker, S.A., Ye, R., Härer, C., Marchetti, C.,
812 Morrice, N., Jeggo, P.A., et al. (2006). DNA-PK autophosphorylation facilitates Artemis
813 endonuclease activity. EMBO J *25*, 3880–3889. 10.1038/sj.emboj.7601255.

814 41. Chan, D.W., and Lees-Miller, S.P. (1996). The DNA-dependent protein kinase is inactivated by
815 autophosphorylation of the catalytic subunit. J Biol Chem *271*, 8936–8941.
816 10.1074/jbc.271.15.8936.

817 42. Reddy, Y.V.R., Ding, Q., Lees-Miller, S.P., Meek, K., and Ramsden, D.A. (2004). Non-homologous
818 end joining requires that the DNA-PK complex undergo an autophosphorylation-dependent
819 rearrangement at DNA ends. J Biol Chem *279*, 39408–39413. 10.1074/jbc.M406432200.

820 43. Block, W.D., Yu, Y., Merkle, D., Gifford, J.L., Ding, Q., Meek, K., and Lees-Miller, S.P. (2004).
821 Autophosphorylation-dependent remodeling of the DNA-dependent protein kinase catalytic
822 subunit regulates ligation of DNA ends. Nucleic Acids Res *32*, 4351–4357. 10.1093/nar/gkh761.

823 44. Goff, N. J., Brenière, M., Buehl, C. J., de Melo, A. J., Huskova, H., Ochi, T., Blundell, T. L., Mao, W.,
824 Yu, K., Modesti, M., & Meek, K. (2022). Catalytically inactive DNA ligase IV promotes DNA repair
825 in living cells. Nucleic Acids Research, 50(19). https://doi.org/10.1093/nar/gkac913

826 45. Jayaram, S., Ketner, G., Adachi, N., & Hanakahi, L. A. (2008). Loss of DNA ligase IV prevents
827 recognition of DNA by double-strand break repair proteins XRCC4 and XLF. Nucleic Acids
828 Research, 36(18). https://doi.org/10.1093/nar/gkn552

829 46. Francis, D. B., Kozlov, M., Chavez, J., Chu, J., Malu, S., Hanna, M., & Cortes, P. (2014). DNA Ligase
830 IV regulates XRCC4 nuclear localization. DNA Repair, 21.
831 https://doi.org/10.1016/j.dnarep.2014.05.010

832 47. Huang, R. X., & Zhou, P. K. (2020). DNA damage response signaling pathways and targets for
833 radiotherapy sensitization in cancer. In Signal Transduction and Targeted Therapy (Vol. 5, Issue
834 1). https://doi.org/10.1038/s41392-020-0150-x

835 48. Groelly, F. J., Fawkes, M., Dagg, R. A., Blackford, A. N., & Tarsounas, M. (2023). Targeting DNA
836 damage response pathways in cancer. In Nature Reviews Cancer (Vol. 23, Issue 2).
837 https://doi.org/10.1038/s41568-022-00535-5

838 49. Cong, L., Ran, F.A., Cox, D., Lin, S., Barretto, R., Habib, N., Hsu, P.D., Wu, X., Jiang, W., Marraffini,
839 L.A., et al. (2013). Multiplex Genome Engineering Using CRISPR/Cas Systems. Science (1979) *339*,
840 819–823. 10.1126/science.1231143.

841 50. Xi, L., Schmidt, J.C., Zaug, A.J., Ascarrunz, D.R., and Cech, T.R. (2015). A novel two-step genome
842 editing strategy with CRISPR-Cas9 provides new insights into telomerase action and TERT gene
843 expression. Genome Biol *16*, 231. 10.1186/s13059-015-0791-1.

844 51. Hoelzel, C. A., & Zhang, X. (2020). Visualizing and Manipulating Biological Processes by Using
845 HaloTag and SNAP-Tag Technologies. In ChemBioChem (Vol. 21, Issue 14).
846 https://doi.org/10.1002/cbic.202000037

847 52. Zhao, C., Teng, E.M., Summers, R.G., Ming, G., and Gage, F.H. (2006). Distinct Morphological
848 Stages of Dentate Granule Neuron Maturation in the Adult Mouse Hippocampus. The Journal of
849 Neuroscience *26*, 3–11. 10.1523/JNEUROSCI.3648-05.2006.

850 53. Neal, J.A., Xu, Y., Abe, M., Hendrickson, E., and Meek, K. (2016). Restoration of ATM Expression in
851 DNA-PKcs-Deficient Cells Inhibits Signal End Joining. J Immunol *196*, 3032–3042.
852 10.4049/jimmunol.1501654.

853 54. Broadbent, D.G., Barnaba, C., Perez, G.I., and Schmidt, J.C. (2023). Quantitative analysis of
854 autophagy reveals the role of ATG9 and ATG2 in autophagosome formation. Journal of Cell
855 Biology *222*. 10.1083/jcb.202210078.

856 55. Laine, R.F., Tosheva, K.L., Gustafsson, N., Gray, R.D.M., Almada, P., Albrecht, D., Risa, G.T., Hurtig,
857 F., Lindås, A.C., Baum, B., et al. (2019). NanoJ: A high-performance open-source super-resolution
858 microscopy toolbox. J Phys D Appl Phys *52*. 10.1088/1361-6463/ab0261.

859 56. Grimm, J.B., English, B.P., Chen, J., Slaughter, J.P., Zhang, Z., Revyakin, A., Patel, R., Macklin, J.J.,
860 Normanno, D., Singer, R.H., et al. (2015). A general method to improve fluorophores for live-cell
861 and single-molecule microscopy. Nat Methods *12*. 10.1038/nmeth.3256.

862 57. Grimm, J.B., Xie, L., Casler, J.C., Patel, R., Tkachuk, A.N., Falco, N., Choi, H., Lippincott-Schwartz, J.,
863 Brown, T.A., Glick, B.S., et al. (2021). A General Method to Improve Fluorophores Using
864 Deuterated Auxochromes. JACS Au *1*. 10.1021/jacsau.1c00006.

865 58. Klump, B.M., Perez, G.I., Patrick, E.M., Adams-Boone, K., Cohen, S.B., Han, L., Yu, K., and Schmidt,
866 J.C. (2023). TCAB1 prevents nucleolar accumulation of the telomerase RNA to facilitate
867 telomerase assembly. Cell Rep *42*, 112577. 10.1016/j.celrep.2023.112577.

868

869

870

SUPPLEMENTAL MATERIAL

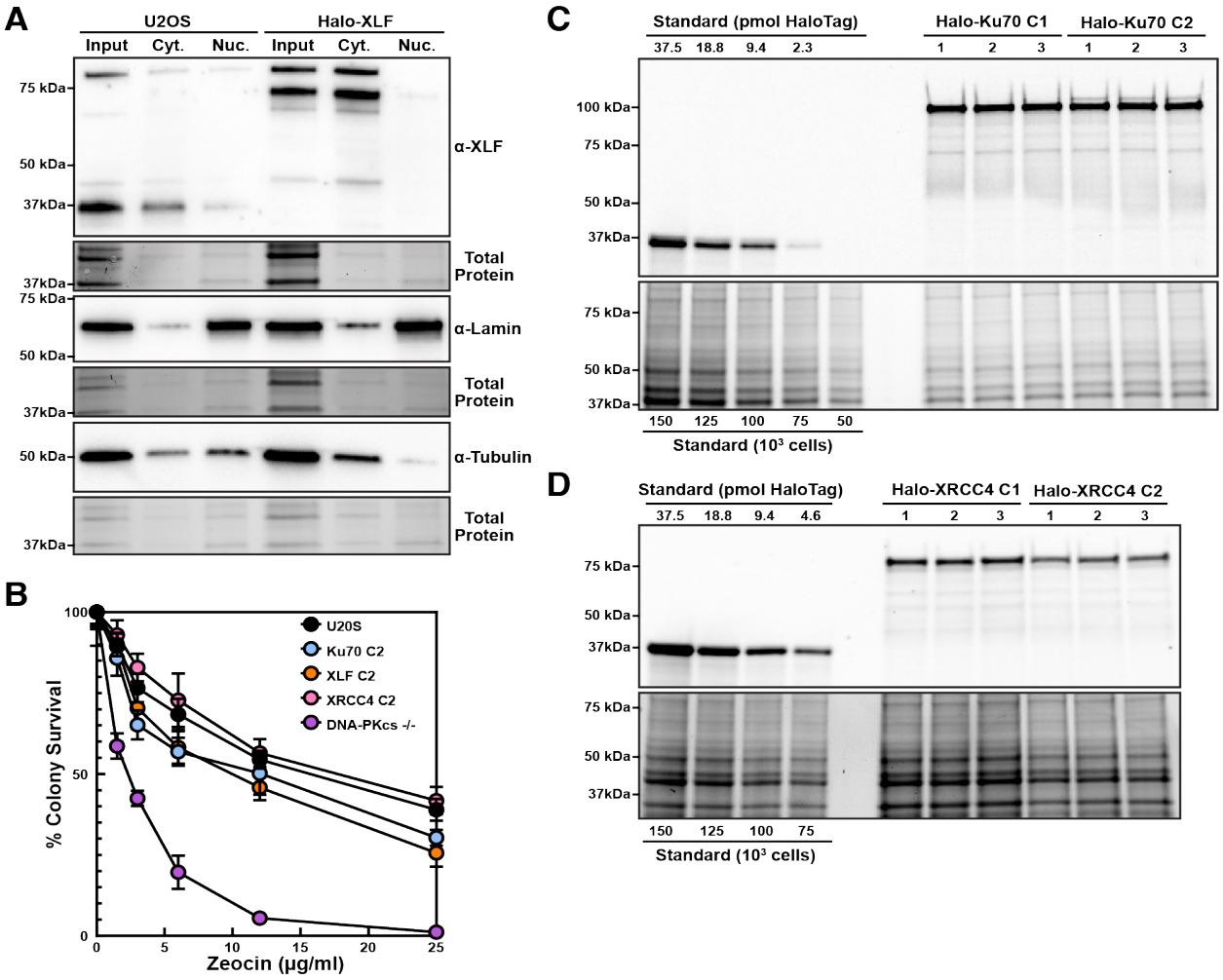

Supplemental Figure 1. Analysis of sub-cellular localization, functionality, and total abundance of HaloTagged DNA repair factors. (A) Western blot analysis of cytoplasmic (Cyt.) and nuclear (Nuc.) fractions from parental U20S and Halo-XLF cells probed with antibodies against XLF, Lamin (nuclear marker), and Tubulin (cytoplasmic marker). **(B)** Clonogenic survival assay of of a second independent clone of for all U2OS cells expressing HaloTagged NHEJ factors, parental U2OS cells, and U2OS cells with DNA-PKcs knockout after challenge with zeocin (N = 4, 3 technical replicates per biological replicate, Mean ± S.D.). **(C-D)** Fluorescence imaging (JF646) and total protein staining for two clones of **(C)** Halo-Ku70 and **(D)** Halo-XRCC4 expressing cells, alongside a protein standard containing a known amount of recombinant 3xFLAG-HaloTag protein labeled with JF646 and whole cell lysate of a known number of cells.

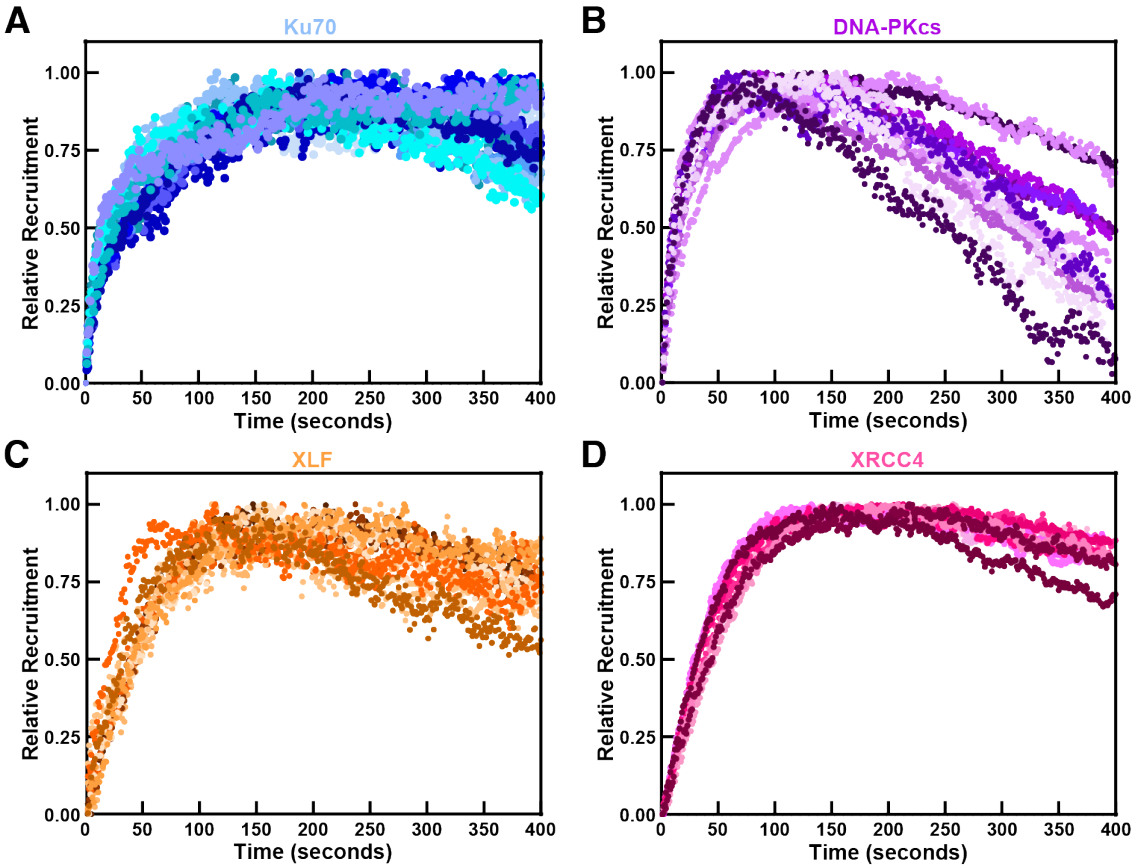

Supplemental Figure 2. Analysis of HaloTagged NHEJ factor recruitment to LMI induced DNA lesions. (A-D) Plots showing normalized fluorescence intensity and recruitment of **(A)** Halo-Ku70, **(B)** Halo-DNA-PKcs, **(C)** Halo-XLF, and **(D)** Halo-XRCC4 to laser-induced DNA lesions. Each shade represents data from an individual cell that was analyzed, and the fluorescence intensity was normalized to the brightest frame of each accumulation curve.

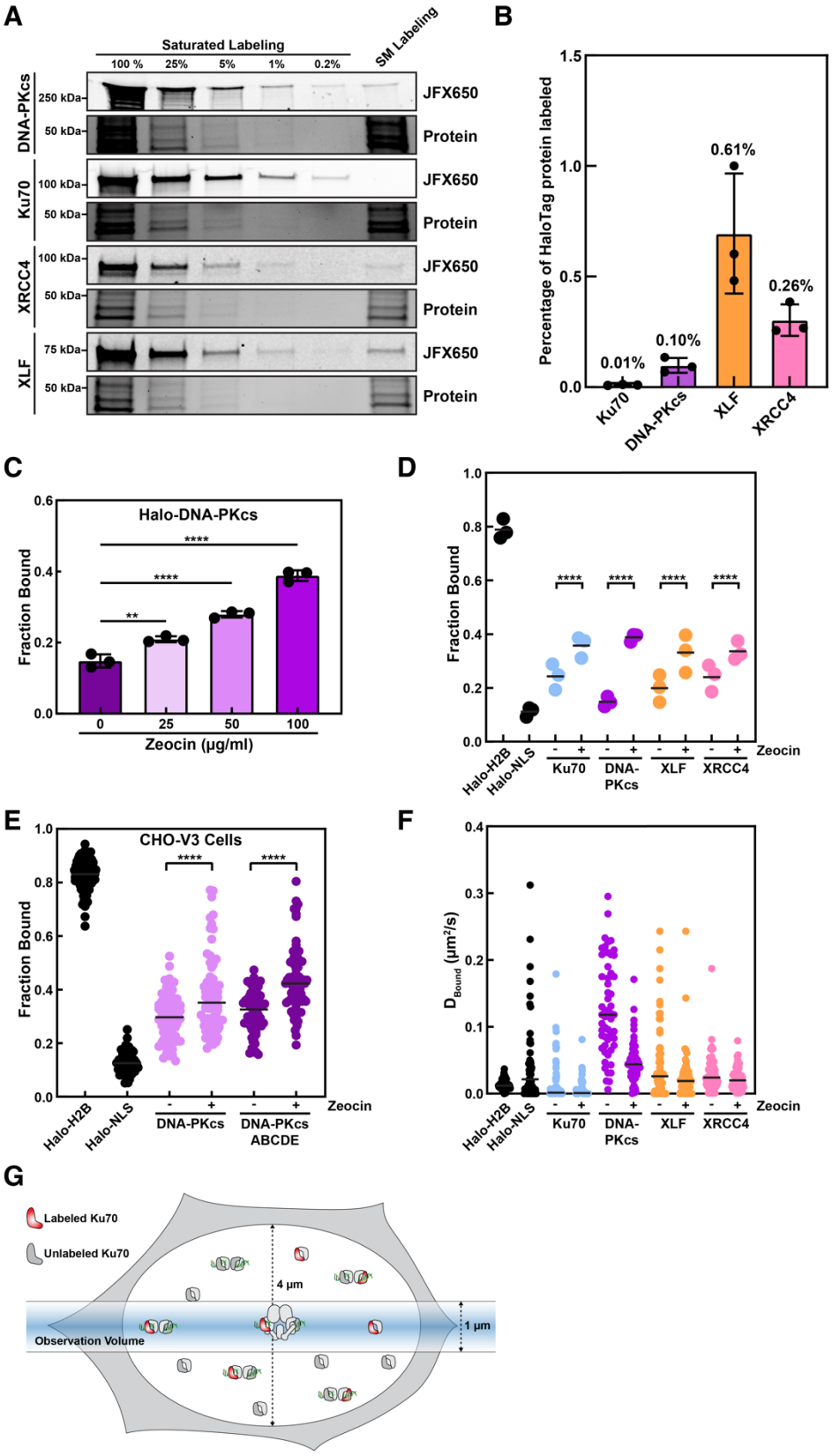

Supplemental Figure 3. Labeling analysis and single-particle tracking of HaloTagged NHEJ factors. (A) Fluorescence imaging and total protein staining of an SDS-PAGE gel with a standard of each HaloTagged NHEJ factor

after labeling under saturation conditions (30 minutes, 100 nM HaloTag ligand) or partial labeling for single-molecule imaging (30 seconds for Halo-Ku70, 1 minute for Halo-DNA-PKcs, Halo-XRCC4, and Halo-XLF, 10 nM HaloTag ligand) with JFX650 HaloTag ligand. **(B)** Quantification of the fluorescence intensity normalized to total protein loading for the gels shown in **(A)** (Mean ± S.D.**)**. **(C)** Fraction bound of Halo-DNA-PKcs in the presence of increasing amounts of Zeocin. Each data point represents the Spot-On fit of the pooled data from all cells in a biological replicate (N = 3, n ≥ 20 cells for each protein per replicate and condition, Black bar = median). Data were analyzed by two-way ANOVA with Tukey's posthoc test (** = $p < 0.01$, **** = $p < 0.0001$)**. (D)** Plot of the Fraction Bound for each HaloTag NHEJ protein under untreated conditions and post-Zeocin exposure that were analyzed using a two-state model of diffusion. Each data point represents pooled data from all cells in a biological replicate. (N = 3, n ≥ 20 cells for each protein per replicate and condition, Black bar = median). Data were analyzed by two-way ANOVA with Tukey's posthoc test (**** = $p < 0.0001$)**.** Same data presented in Figure 3B but analyzed by Spot-On using the pooled step size distribution from all cells for each biological replicate. **(E)** Plot of the Fraction Bound for Halo-DNA-PKcs wild type and Halo-DNA-PKcs ABCDE mutant transiently expressed in CHO-V3 cells under untreated conditions and post-Zeocin exposure that were analyzed using a two-state model of diffusion. Each dot represents the fraction bound of each protein in an individual cell (N = 3, n ≥ 20 cells for each protein per replicate and condition, Black bar = median). Data were analyzed by two-way ANOVA with Tukey's posthoc test (**** = $p < 0.0001$)**. (F)** Diffusion coefficients of static molecules of HaloTag DDR proteins. Each data point represents the D_{Bound} calculated from the tracks in an individual cell (N = 3, n ≥ 20 cells for each protein per replicate and condition, Black bar = median). **(G)** Graphical rational for the calculation of the total number of breaks bound by the DNA repair factors in the single-molecule imaging experiments.

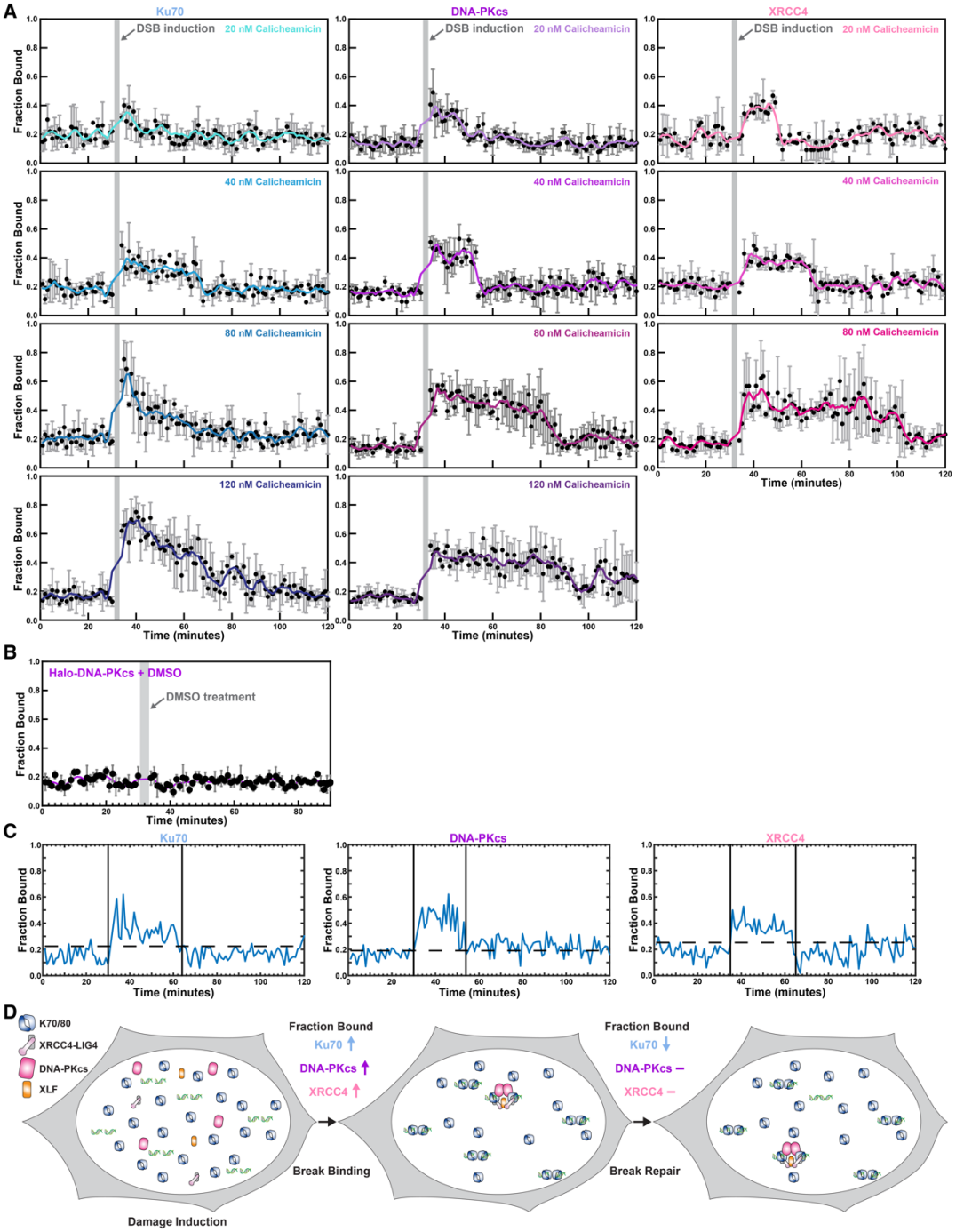

Supplemental Figure 4. Labeling analysis and single-particle tracking of HaloTagged NHEJ factors. (A) Plot of the static fraction of Halo-Ku70, Halo-DNA-PKcs, and Halo-XRCC4 before and after DNA damage induction (shaded area) with various concentrations of Calicheamicin for 3 minutes (N = 3, Mean ± S.D). Lines represent the rolling average over three consecutive timepoints. **(B)** Plot of the static fraction of Halo-DNA-PKcs after treatment with DMSO for 3 minutes (shaded area, N = 3, Mean ± S.D). **(C)** Quantification of the time window of chromatin association for Halo-Ku70, Halo-DNA-PKcs, and Halo-XRCC4. The time between the vertical bars is considered the binding time, the horizontal dashed bar indicates the binding threshold. **(D)** Model for the consecutive repair of DNA breaks in our time course experiments. Because Ku70 is present in large excess relative to DNA-PKcs and XRCC4 its binding is expected to be reduced when breaks are repaired, while the static fraction of DNA-PKcs and XRCC4 remains constant, when the number of breaks present exceed the number of DNA-PKcs and XRCC4 molecules present in the cell.

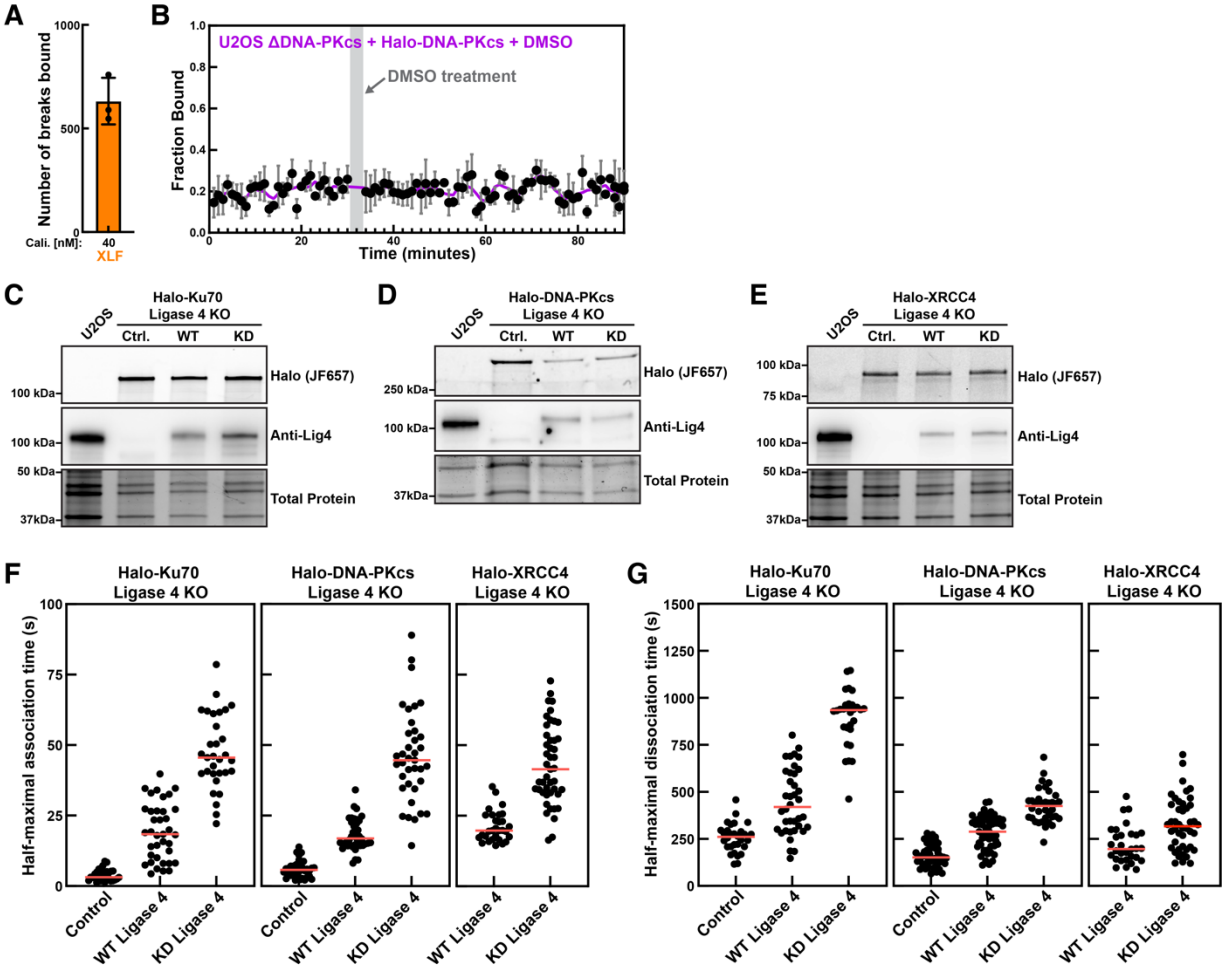

Supplemental Figure 5. Kinetics of chromatin recruitment of Halo-DNA-PKcs under control conditions. (A) Quantification of the number of break bound Halo-XLF (pooled data for 10 time points after chromatin recruitment) molecules after DNA damage induction with 40 nM calicheamicin (N = 3, Mean ± S.D.). **(B)** Plot of the static fraction of Halo-DNA-PKcs in U2OS cells with endogenous DNA-PKcs knocked out and Halo-DNA-PKcs expressed by stable transfection after treatment with DMSO (shaded area, N = 3, Mean ± S.D.). **(C-E)** Fluorescence gels (top), western blots (middle), and total protein stain of cell lysates generated from parental U2OS cells, and U2OS cells expressing **(C)** Halo-Ku70, **(D)** Halo-DNA-PKcs, or **(E)** Halo-XRCC4 labeled with JF657 Halo-ligand in which endogenous ligase 4 was knocked out, transiently transfected with a control vector (Ctrl.) of expression vectors for wildtype ligase 4 (WT) or catalytically inactive ligase 4 (KD). **(F-G)** Half-maximal association **(F)** and dissociation times **(G)** for laser micro irradiation experiments of U2OS cells with ligase 4 knockout, expressing Halo-Ku70 (left), Halo-DNA-PKcs (middle), or Halo-XRCC4 (right), transiently expressing wildtype ligase 4, a vector control, or ligase dead ligase 4 (N = 30-45 cells per condition, Mean). Each data point represents the fit of the data derived from an individual cell. Half-maximal association and dissociation times were fit by using only the data prior or after maximal fluorescence accumulation for each cell, respectively.

937 **SUPPLEMENTAL MOVIE LEGENDS**

938 **Movie S1.** Representative movie demonstrating recruitment of JFX650-labeled 3xFLAG-
939 HaloTagged Ku70 to DNA DSBs after laser microirradiation. Images were acquired at one frame
940 per second.
941

942 **Movie S2.** Representative movie demonstrating recruitment of JFX650-labeled 3xFLAG-
943 HaloTagged-DNA-PKcs to DNA DSBs after laser microirradiation. Images were acquired at one
944 frame per second.
945

946 **Movie S3.** Representative movie demonstrating recruitment of JFX650-labeled 3xFLAG-
947 HaloTagged XRCC4 to DNA DSBs after laser microirradiation. Images were acquired at one
948 frame per second.
949

950 **Movie S4.** Representative movie demonstrating recruitment of JFX650-labeled 3xFLAG-
951 HaloTagged XLF to DNA DSBs after laser microirradiation. Images were acquired at one frame
952 per second.
953

954 **Movie S5.** Representative live-cell single-molecule imaging movie of Halo-NLS transiently
955 expressed in U2OS cells, labeled with JFX650, and acquired at 179 frames per second using
956 the Hamamatsu ORCA BT Fusion camera.
957

958 **Movie S6.** Representative live-cell single-molecule imaging movie of Halo-H2B transiently
959 expressed in U2OS cells, labeled with JFX650, and acquired at 179 frames per second using
960 the Hamamatsu ORCA BT Fusion camera.
961

962 **Movie S7.** Representative live-cell single-molecule imaging movie of 3xFLAG-HaloTagged
963 Ku70 in a control cell (left) and a cell treated with zeocin (right), labeled with JFX650, and
964 acquired at 146 frames per second using the Andor 897 Ultra camera.
965

966 **Movie S8.** Representative live-cell single-molecule imaging movie of 3xFLAG-HaloTagged XLF
967 in a control cell (left) and a cell treated with zeocin (right), labeled with JFX650, and acquired at
968 146 frames per second using the Andor 897 Ultra camera.
969

970 **Movie S9.** Representative live-cell single-molecule imaging movie of 3xFLAG-HaloTagged
971 XRCC4 in a control cell (left) and a cell treated with zeocin (right), labeled with JFX650, and
972 acquired at 146 frames per second using the Andor 897 Ultra camera.
973
974 **Movie S10.** Representative live-cell single-molecule imaging movies of 3xFLAG-HaloTagged
975 DNA-PKcs labeled with JFX650 before and after treatment with calicheamicin, acquired at 179
976 frames per second using the Hamamatsu ORCA Fusion BT camera.
977
978 **Movie S11.** Representative single-molecule imaging movie of Halo-Ku70 in Ligase 4 knockout
979 out cells expressing wild-type Ligase 4 (top row), a vector control (middle row), or catalytically
980 inactive Ligase 4 (bottom row) before DNA damage induction with calicheamicin (left column),
981 immediately after DNA damage induction (middle column), and 35 minutes after DNA damage
982 induction (right column) imaged at 171 frames per second using the Hamamatsu ORCA Fusion
983 BT camera.
984
985 **Movie S12.** Representative single-molecule imaging movie of Halo-DNA-PKcs in Ligase 4
986 knockout out cells expressing wild-type Ligase 4 (top row), a vector control (middle row), or
987 catalytically inactive Ligase 4 (bottom row) before DNA damage induction with calicheamicin
988 (left column), immediately after DNA damage induction (middle column), and 35 minutes after
989 DNA damage induction (right column) imaged at 171 frames per second using the Hamamatsu
990 ORCA Fusion BT camera.
991
992 **Movie S13.** Representative single-molecule imaging movie of Halo-XRCC4 in Ligase 4
993 knockout out cells expressing wild-type Ligase 4 (top row), a vector control (middle row), or
994 catalytically inactive Ligase 4 (bottom row) before DNA damage induction with calicheamicin
995 (left column), immediately after DNA damage induction (middle column), and 35 minutes after
996 DNA damage induction (right column) imaged at 171 frames per second using the Hamamatsu
997 ORCA Fusion BT camera.
998
999 **Movie S14.** Representative laser micro-irradiation movie of Halo-Ku70 in Ligase 4 knockout out
1000 cells expressing wild-type Ligase 4 (left panel), a vector control (middle panel), or catalytically
1001 inactive Ligase 4 (right panel) imaged at 1 frame per second using the Hamamatsu ORCA
1002 Fusion BT camera.
1003

1004 **Movie S15.** Representative laser micro-irradiation movie of Halo-DNA-PKcs in Ligase 4
1005 knockout out cells expressing wild-type Ligase 4 (left panel), a vector control (middle panel), or
1006 catalytically inactive Ligase 4 (right panel) imaged at 1 frame per second using the Hamamatsu
1007 ORCA Fusion BT camera.
1008
1009 **Movie S16.** Representative laser micro-irradiation movie of Halo-XRCC4 in Ligase 4 knockout
1010 out cells expressing wild-type Ligase 4 (left panel), a vector control (middle panel), or
1011 catalytically inactive Ligase 4 (right panel) imaged at 1 frame per second using the Hamamatsu
1012 ORCA Fusion BT camera.5
1013